*J. Fluid Mech.* (2010), *vol.* 661, *pp.* 262–293. 
doi:10.1017/S0022112010002934

# Towards the development of a multiscale, multiphysics method for the simulation of rarefied gas flows

DAVID A. KESSLER†, ELAINE S. ORAN AND CAROLYN R. KAPLAN

Laboratory for Computational Physics and Fluid Dynamics, US Naval Research Laboratory, Washington, DC 20375, USA

(Received 6 May 2009; revised 21 May 2010; accepted 21 May 2010; first published online 2 August 2010)

We introduce a coupled multiscale, multiphysics method ($CM^3$) for solving for the behaviour of rarefied gas flows. The approach is to solve the kinetic equation for rarefied gases (the Boltzmann equation) over a very short interval of time in order to obtain accurate estimates of the components of the stress tensor and heat-flux vector. These estimates are used to close the conservation laws for mass, momentum and energy, which are subsequently used to advance continuum-level flow variables forward in time. After a finite time interval, the Boltzmann equation is solved again for the new continuum field, and the cycle is repeated. The target applications for this type of method are transition-regime gas flows for which standard continuum models (e.g. Navier–Stokes equations) cannot be used, but solution of Boltzmann's equation is prohibitively expensive. The use of molecular-level data to close the conservation laws significantly extends the range of applicability of the continuum conservation laws. In this study, the $CM^3$ is used to perform two proof-of-principle calculations: a low-speed Rayleigh flow and a thermal Fourier flow. Velocity, temperature, shear-stress and heat-flux profiles compare well with direct-simulation Monte Carlo solutions for various Knudsen numbers ranging from the near-continuum regime to the transition regime. We discuss algorithmic problems and the solutions necessary to implement the $CM^3$, building upon the conceptual framework of the heterogeneous multiscale methods.

**Key words:** computational methods, gas dynamics, kinetic theory

## 1. Introduction

A variety of physical models, ranging from those that describe basic molecular interactions governed by Newton's laws to those that use continuum approximations, are commonly used to treat gas flows. This hierarchy of models provides successively more detailed information about the underlying physics. The regions of validity of these models are described by sets of physical parameters, such as the Knudsen number or the Mach number. When the regions of validity of these parameters overlap, more than one model can be used (Oran, Oh & Cybyk 1998).

† Email address for correspondence: dakessle@lcp.nrl.navy.mil

For gas flows, the Knudsen number is an important parameter for determining how molecular-level interactions affect the continuum-level transport of momentum and energy. It is defined as $Kn = \lambda/L$, where $\lambda$ is the mean free path of the gas molecules and $L = \phi/|\partial\phi/\partial x|$ is a length scale associated with the spatial variation in the macroscopic flow properties, $\phi$. When $Kn$ is small, there are enough molecular collisions for the gas to be described by a continuum model, and the Navier–Stokes equations can be used. For large values of $Kn$, the constitutive models used in the Navier–Stokes equations break down, and the kinetic theory of gases must be used. For sufficiently dilute gases, i.e. for which molecular collisions can be assumed to be binary, Boltzmann's equation is commonly used to describe the flow (Cercignani 1975). Many gas flows of engineering interest fall into the overlapping region of validity of Boltzmann's and Navier–Stokes equations, which we call the transition regime, and here we restrict our discussion to such flows.

Boltzmann's equation is an integro-differential equation in phase space for the quantity $F = nf$, where $n$ is the number density of molecules and $f$ is the single-particle velocity-distribution function. Analytical solutions exist only for the simplest of cases, and numerical simulations are expensive. Various direct-solution methods exist, such as the Hicks–Yen–Nordsieck hybrid approach (Nordsieck & Hicks 1967; Yen 1971), which uses a finite-difference method to discretize phase space and a Monte Carlo method to calculate the collision integral. A review of the literature of the early development of such direct-solution methods can be found in the article by Yen (1984). Linearization and other approximation techniques for the collision integral, such as the Bhatnagar–Gross–Krook (BGK) model (Cercignani 1975), can simplify the Boltzmann equation and allow tractable analytical representations for low-$Kn$ flows. These equations have been successful in a number of configurations and are widely used, but they can be difficult to solve for large values of $Kn$. Other solution approaches based on a discrete-velocity model (Broadwell 1964; Gatignol 1970; Goldstein, Sturtevant & Broadwell 1989) restrict the allowable velocities to a few selected ranges and have been shown to provide qualitatively correct solutions for a number of test flows. More recent developments in discrete-velocity modelling have been discussed by Andullah & Babovsky (2003), Mieussens (2000) and Babovsky (1998).

Perhaps the most common solution approach is to simulate the flow using methods that treat the gas molecules as discrete particles and explicitly track their trajectories. The direct-simulation Monte Carlo (DSMC) method (Bird 1994) calculates the trajectories of statistically representative particles, each representing the collective behaviour of a large number of individual molecules. DSMC has been shown to be equivalent to solving the Boltzmann equation as the simulation time step is reduced to zero (Wagner 1992). This method has been successful at simulating a wide variety of low-density (large-$\lambda$) gas flows. For dense and moderately dense flows, DSMC is inefficient because of cell size and time-step limitations. Each cell must be a fraction of $\lambda$, which is quite small for dense gases. Since each cell must contain enough particles to obtain a good statistical representation of the gas, the computational costs of DSMC increase drastically as the density increases. Similarly, the mean time between collisions decreases with decreasing $\lambda$, which restricts the size of each time step. Other discrete methods approximate continuous trajectories of particles in phase space by discrete movements along a fixed lattice. These lattice-gas methods have been used in the context of the Boltzmann equation (McNamara & Zanetti 1988; Higuera & Jimenez 1989; Benzi, Succi & Vergassola 1992) and the BGK equation (Qian, d'Humières & Lallemand 1992). A more general discussion of lattice-gas methods was given by

Doolen (1990). Recent advances in energy conservation (Ansumali & Karlin 2005), boundary conditions (Ansumali & Karlin 2002; Watari 2009) and Galilean invariance (Chikatamarla & Karlin 2006) for lattice-Boltzmann methods have generated interest in using these methods for finite-$Kn$ flows (Shen *et al.* 2004; Ansumali *et al.* 2007; Kim, Pitsch & Boyd 2008; Verhaeghe, Luo & Blanpain 2009).

The continuum-level equations that govern the bulk flow, the conservation of mass, momenta and energy are easier to analyse and solve numerically than the Boltzmann equation. The downside is that closure models are necessary to describe how the molecular-level motions affect the continuum-level transport of momentum and energy. Closure has been derived in a variety of ways. Chapman and Enskog constructed an asymptotic expansion of the distribution function about the equilibrium distribution as a power series in $Kn$. Solution of the $O(Kn)$ problem yields the usual Navier–Stokes–Fourier model, which gives the viscous stress tensor and heat-flux vector as linear functions of the flow variables and their gradients. The resulting Navier–Stokes equations are accurate for a wide variety of flows and are used almost exclusively in the field of fluid dynamics. Higher-order closures based on the Chapman–Enskog approach, such as the Burnett ($O(Kn^2)$) and super-Burnett ($O(Kn^3)$) equations, exist, but they also require closure. The use of simple constitutive laws for the unspecified higher-order tensors in these equations can sometimes lead to solutions that provide a more accurate description of gas flows than the Navier–Stokes equations (Pham-Van-Diep, Erwin & Muntz 1991) and can be used for larger $Kn$ flows (Fiscko & Chapman 1989). An alternative approach is to derive governing equations for the additional eight moments that determine the viscous stress tensor and heat-flux vector. Grad's original 13-moment closure (Grad 1949), and, later, dynamic corrections to these moment equations (Karlin *et al.* 1998; Struchtrup & Torrilhon 2003; Torrilhon & Struchtrup 2004), are between second and fourth order in accuracy (in terms of $Kn$). There are difficulties associated with the use of these higher-order continuum models. The degree to which they extend the validity of the continuum approach is not well understood. Also, there is no standard way of treating boundary conditions for the higher moments that arise in these formulations. The end result is that there is an upper bound on $Kn$ above which continuum models cannot be used.

Thus, for a range of $Kn$, it is prohibitively expensive to solve the Boltzmann equation for the molecular-level behaviour, but continuum modelling of these processes is inaccurate. This paper suggests taking a different approach, one in which the physical processes occurring on multiple, potentially disparate scales of the system are independently computed and combined. By solving the molecular-level equations only on the space and time scales for which they are relevant, it may be possible to gain computational efficiency over using them to describe the entire flow. The general framework of this approach has been laid out by E & Engquist (2003), who described these types of methods as the heterogeneous multiscale methods (HMM). They identified two classes of HMM: (i) situations in which a macroscopic model is known but ceases to be valid in localized regions of space or time and (ii) situations for which a macroscopic model is not explicitly known, but is known to exist. The first class of HMM is most relevant to this discussion since both the microscopic (Boltzmann) and continuum-level (Navier–Stokes) equations are known. Two general types of multiscale methods have been used to calculate flows in the transition regime.

In the first type, commonly referred to as spatial hybrid methods (Wadsworth & Erwin 1992; Garcia *et al.* 1999; Roveda, Goldstein & Varghese 2000; Wijesinghe *et al.*

2004; Lian *et al.* 2005; Schwartzentruber & Boyd 2006), a continuum breakdown parameter is used to determine in which regions the Navier–Stokes equations are valid. In these regions, traditional methods of solving the continuum-level equations are used. In regions where the Navier–Stokes equations are not valid, DSMC is used to calculate the flow. Special procedures are used to couple the flow fields in the areas of overlap between the separate regions (Bourgat, Le Tallec & Tidriri 1996; Le Tallec & Mallinger 1997). A variation of this technique uses adaptive mesh refinement to dynamically control the grid size and automatically uses DSMC in regions where the finest grid sizes are used (Garcia *et al.* 1999; Wijesinghe *et al.* 2004). Other domain-decomposition techniques have been introduced in which the coupling between the continuum and kinetic regions is done through the equations rather than by matching boundary conditions between the domains (Degond & Jin 2005; Degond, Jin & Mieussens 2005).

In the second type of multiscale methods, information about the microscopic system is used to form a new set of macroscopic evolution equations. One example is the coarse-grained acceleration method for the Boltzmann equation (Al-Mohssen, Hadjiconstantinou & Kevrekidis 2007). This method, based on the 'equation-free' simulation framework (Theodoropoulos, Qian & Kevrekidis 2000; Kevrekidis *et al.* 2003; Kevrekidis, Gear & Hummer 2004), uses a variance-reduction Monte Carlo method (Baker & Hadjiconstantinou 2005) to solve the nonlinear Boltzmann equation for a short period of time to obtain an accurate description of the rate of change of the continuum-level velocity field. The continuum solution is then updated based on the rate of change of the average flow calculated using the microscale data, and the process is repeated until the flow field reaches a steady state. A second example, the micro–macro upscaling model (Degond, Liu & Mieussens 2006), uses a new set of macroscopic equations that include effects due to localized 'upscaling' of the kinetic equations. Here the term upscaling refers to the incorporation of terms that depend on the perturbation of the velocity distribution from equilibrium. In regions where the molecular velocity distribution function is equal to the equilibrium distribution, the equations reduce to the typical hydrodynamic equations. A third example, the gas-kinetic hydrodynamic method (Prendergast & Xu 1993; Xu & Prendergast 1994), uses basic ideas from the kinetic theory and the BGK equation to calculate the continuum-level fluxes as moments of an approximation of the velocity-distribution function. These fluxes are used to advance the continuum-level equations forward in time using the Navier–Stokes or Euler equations. Other methods of this type, termed 'Boltzmann-type schemes' (Harten, Lax & van Leer 1983), such as the beam method (Sanders & Prendergast 1974), the Steger–Warming method (Steger & Warming 1981), the equilibrium flux method (Pullin 1980) and others (Reitz 1981; van Albada, van Leer & Roberts 1982; Deshpande 1986; Macrossan 1989; Perthame 1992) combine elements of kinetic theory based on knowledge of the equilibrium distribution function with the continuum-level fluxes to solve the Euler equations, and are thus limited to inviscid or nearly inviscid flows.

In this paper, we describe a new multiscale approach, which we call the coupled, multiscale, multiphysics method ($CM^3$). We then discuss problems and the proposed solutions associated with its implementation, and show several proof-of-principle calculations. In this approach, continuum-level conservation laws are used to project the mass, momentum and energy forward in time. The projection uses approximations of the unclosed terms that have been calculated directly from the Boltzmann equation. Since this approach uses a better approximation to the velocity-distribution function $f$ to compute the unclosed terms in the conservation laws than perturbation methods

that require $Kn$ to be small, it should be accurate over a much broader range of gas flows. Although similar methods have been used to calculate the viscoelastic flow of polymeric solutions (Laso & Ottinger 1993; Yasuda & Yamamoto 2010) and dendritic solidification (Plapp & Karma 2000), we discuss for the first time how this methodology can be applied to rarefied gas flows.

Potentially, there are two advantages that might be gained by using this type of approach. First, since the continuum variables are always accessible when using CM$^3$, it could be seamlessly integrated into a spatial hybrid method to solve the rarefied portions of the domain in the place of DSMC. Doing so would eliminate the need for using complicated coupling procedures between DSMC regions and Navier–Stokes regions. Second, if the conservation laws modified by the approximated closures satisfy certain mathematical constraints, it should be possible to take relatively large advancements in time using computationally efficient methods for solving the coupled partial differential equations. These constraints are that solutions to these equations should lie on the same manifold as solutions to the exact conservation laws. The overall efficiency of this approach is tied to how easily $f$ can be approximated. Here we use a Monte Carlo method that is a slight variation of the DSMC method to generate successively more accurate estimates of $f$.

In this paper, we take the first steps towards realizing these advantages by showing how the CM$^3$ can be used to solve apparently simple one-dimensional test flows. This allows us to develop the basic methodology of the multiscale procedure, and in doing so, has revealed a variety of physical and algorithmic challenges. The identification and resolution of these issues forms the basis of this study. In the future, we would like to couple the CM$^3$ to a standard computational fluid dynamics code to produce a more efficient spatial hybrid method. This, however, requires a number of extensions to the method. Some smaller issues, such as the extension to multiple dimensions, and larger issues, such as the development of well-posed inflow and outflow boundary conditions, still need to be addressed. We mention these issues here in the hope of stimulating future research in this area.

This paper is organized as follows. In § 2, we introduce the test flows and describe the physical models that govern the systems and the methodology for computing solutions using the multiscale approach. The steady-state solutions to the test problems calculated using the multiscale method are compared to solutions obtained using standard DSMC in § 3. We then discuss the issues associated with obtaining these solutions and give a basic analysis of the efficiency of the multiscale algorithm in § 4. Finally, we discuss ways to improve the method and identify areas where more analysis will be needed to produce a mature computational algorithm in § 5.

## 2. Multiscale model and solution algorithm

### 2.1. *Models*

Consider an unsteady Rayleigh flow in which two parallel plates, one at $z = 0$ and the other at $z = 10^{-4}$ m, infinite in extent in the $x$- and $y$-directions, are separated by a homogeneous, isothermal gas. At time $t = 0$, the bottom plate is impulsively set in motion with a velocity $V$ in the $x$-direction, and the temperature is adjusted to $T_1$, while the top plate is held stationary at temperature $T_2$, as depicted in figure 1. The Knudsen number of the flow is varied by changing the static pressure and thus the density of the gas molecules. Three different static pressures corresponding to three different values of $Kn$ are considered: $P = 7.711 \times 10^{-2}$, $7.711 \times 10^{-3}$ and $1.542 \times 10^{-3}$ atm. We take the gas to be helium, a simple and monatomic gas, which

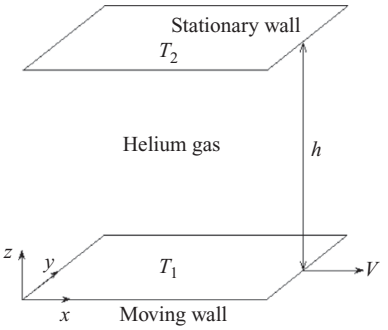


FIGURE 1. Geometry of the nominally one-dimensional test problem considered.

has no rotational or vibrational degrees of freedom. At $T = 273.15\,\mathrm{K}$, the mean free paths of the helium molecules at these pressures are $\lambda = 2 \times 10^{-6}$, $2 \times 10^{-5}$ and $1 \times 10^{-4}$ m, respectively. Using $h$ as the reference length, $Kn = 0.02$, 0.2 and 1.0 for these systems.

2.1.1. *Continuum-level model*

The continuum-level equations that govern the gas flow are conservation of mass, momenta and energy,

$$\frac{\partial \rho}{\partial t} + \nabla \cdot (\rho \boldsymbol{u}_0) = 0, \tag{2.1}$$

$$\frac{\partial}{\partial t}(\rho \boldsymbol{u}_0) + \nabla \cdot (\rho \boldsymbol{u}_0 \boldsymbol{u}_0) = -\nabla P + \nabla \cdot \boldsymbol{\tau}, \tag{2.2}$$

$$\frac{\partial}{\partial t}(\rho e) + \nabla \cdot (\boldsymbol{u}_0 \rho e) = -\nabla \cdot (P \boldsymbol{u}_0) + \nabla \cdot (\boldsymbol{\tau} \cdot \boldsymbol{u}_0) - \nabla \cdot \boldsymbol{q}, \tag{2.3}$$

where $u$, $v$ and $w$ are the $x$-, $y$- and $z$-components of the continuum-level velocity field $\boldsymbol{u}_0$, $\rho$ is the mass density, $e$ is the total energy and $P$ is the local pressure. For a perfect gas, the mass density and temperature are related to the pressure and total energy by the state equations, $P = \rho RT$ and $\rho e = 1/2 \rho u_0^2 + P/(\gamma - 1)$, where $R$ is the specific gas constant and $\gamma$ is the specific heat ratio for the particular gas. The viscous stress tensor $\boldsymbol{\tau}$ and the heat-flux vector $\boldsymbol{q}$ do not, in general, depend on the primitive variables, and, hence, the governing equations do not form a closed set.

The Navier–Newton viscosity model, $\boldsymbol{\tau} = -2/3(\mu(\nabla \cdot \boldsymbol{u}_0)\boldsymbol{I} + 2\mu[1/2(\nabla \boldsymbol{u}_0 + \nabla \boldsymbol{u}_0^T)]$, and Fourier's model of heat conduction, $\boldsymbol{q} = -k \nabla T$, are often used to close the conservation laws. The coefficients of viscosity and heat conduction, $\mu$ and $k$, are properties of the particular fluid. The resulting equations are the compressible Navier–Stokes equations that are commonly used in continuum fluid dynamics (Panton 1996). These models are known to break down for large $Kn$, which means that the Navier–Stokes equations are invalid in this flow regime.

2.1.2. *Molecular-level model*

From the microscopic viewpoint, the distribution of molecular velocities, $f$, in a dilute gas is governed by Boltzmann's equation (Bird 1994),

$$\frac{\partial}{\partial t}(nf) + \boldsymbol{c} \cdot \frac{\partial}{\partial \boldsymbol{r}}(nf) = \int_{-\infty}^{\infty} \int_{0}^{4\pi} n^2 (f^* f_1^* - f f_1) c_r \sigma \, \mathrm{d}\Omega \, \mathrm{d}\boldsymbol{c}_1, \tag{2.4}$$

where $n$ is the number density of molecules and $\boldsymbol{c}$ is the molecular velocity. In this formulation, $f = f(\boldsymbol{c}, \boldsymbol{r}, t)$ is a function of velocity, space and time, while $n = n(\boldsymbol{r}, t)$ is

a function of space–time only. The right-hand side of (2.4) represents the collision of gas molecules of class $\boldsymbol{c}$ with those of class $\boldsymbol{c}_1$ expressed as an integral over velocity space, where $c_r$ is the magnitude of the relative velocity between the molecules, $\sigma$ is the collision cross-section and $\Omega$ is the solid angle of integration. The starred variables indicate post-collision values and those without stars are pre-collision quantities. Macroscopic, or continuum-level, properties of the flow can be calculated by taking moments of $f$. For instance, the mass density, linear momenta and total energy,

$$\rho = \overline{nm_w} = \int_{-\infty}^{\infty} nm_w f \, \mathrm{d}\boldsymbol{c}, \tag{2.5}$$

$$\rho \boldsymbol{u}_o = \rho \overline{\boldsymbol{c}} = \int_{-\infty}^{\infty} nm_w \boldsymbol{c} f \, \mathrm{d}\boldsymbol{c}, \tag{2.6}$$

$$\rho e = \rho \overline{c^2}/2 = \int_{-\infty}^{\infty} \tfrac{1}{2} nm_w c^2 f \, \mathrm{d}\boldsymbol{c}, \tag{2.7}$$

are moments of the molecular mass $m_w$, momenta $m_w\boldsymbol{c}$ and energy $m_w c^2/2$, respectively.

2.1.3. *Multiscale model*

Equations (2.5)–(2.7) can be used to derive a set of conservation laws identical in form to (2.1)–(2.3). Multiply (2.4) by $m_w$, $m_w\boldsymbol{c}$ and $m_w c^2/2$, and integrate over all velocity space. If we assume that the molecular collisions are elastic (i.e. mass, momenta and energy are conserved for each collision) and we decompose $\boldsymbol{c}$ into the sum of the mean velocity $\boldsymbol{u}_0$ and a fluctuating or thermal velocity $\boldsymbol{c}'$, the right-hand side of each equation vanishes and we are left with

$$\frac{\partial \rho}{\partial t} + \nabla \cdot (\rho \boldsymbol{u}_0) = 0, \tag{2.8}$$

$$\frac{\partial}{\partial t}(\rho \boldsymbol{u}_0) + \nabla \cdot (\rho \boldsymbol{u}_0 \boldsymbol{u}_0) + \nabla \cdot (\rho \overline{\boldsymbol{c}'\boldsymbol{c}'}) = 0, \tag{2.9}$$

$$\frac{\partial}{\partial t}(\rho e) + \nabla \cdot (\boldsymbol{u}_0 \rho e) + \nabla \cdot (\rho \overline{\boldsymbol{c}'\boldsymbol{c}'} \cdot \boldsymbol{u}_0) + \nabla \cdot \left(\tfrac{1}{2}\rho \overline{\boldsymbol{c}' c'^2}\right) = 0. \tag{2.10}$$

The additional terms on the left-hand side of the equations represent the effect of the small-scale fluctuating motions of the molecules on the large-scale macroscopic behaviour of the fluid. In the Navier–Stokes equations, these effects are buried in the constitutive models for $\boldsymbol{\tau}$ and $\boldsymbol{q}$. Comparing (2.1)–(2.3) with (2.8)–(2.10) gives the expressions

$$\boldsymbol{\tau} = -(\rho \overline{\boldsymbol{c}'\boldsymbol{c}'} - P\boldsymbol{I}), \tag{2.11}$$

$$\boldsymbol{q} = \tfrac{1}{2}\rho \overline{c'^2 \boldsymbol{c}'}, \tag{2.12}$$

where the pressure $P = \rho \overline{c'^2}/3$. The Chapman–Enskog perturbation theory shows that (2.11)–(2.12) are equivalent to the Navier–Newton viscosity model and Fourier's conduction model, respectively, to first order in $Kn$ for particular values of $\mu$ and $k$. Thus, (2.8)–(2.10) are equal to the Navier–Stokes equations in the limit of small $Kn$. The principal idea presented here is to obtain an approximation for $f$ by solving Boltzmann's equation over a very short time interval for given continuum-level fields of density, momentum and energy. Once $f$ is known at some time $t$, (2.11)–(2.12) can be solved explicitly for $\boldsymbol{\tau}$ and $\boldsymbol{q}$ as functions of space. The results can then be used to close (2.2) and (2.3) and advance the continuum fields forward in time.

### 2.2. *Solution algorithms*

We calculate the flow fields in the gap between the plates using three different methods: indirect solution of the Boltzmann equation using DSMC (Bird 1994), solution of the Navier–Stokes equations using the LCPFCT-finite-volume method (Oran & Boris 2001) and solution of the general conservation laws (see (2.8)–(2.10)) using the multiscale method described in § 2.1.3. In all of the calculations that follow, the flow field is divided into 200 cells in the $z$-direction and 3 cells in the $x$- and $y$-directions, so that $\Delta x = \Delta y = \Delta z = 5 \times 10^{-7}$ m.

### 2.3. *Direct-simulation Monte Carlo method*

The DSMC method (Bird 1994) is used to simulate the behaviour of the gas molecules. The domain is divided into cubic cells with dimension less than or equal to $\lambda/4$ ($\Delta x = \lambda/4$, $\lambda/40$ and $\lambda/200$ for $Kn = 0.02$, 0.2 and 1, respectively). Collision partners are chosen at random in each cell. We employ the variable-hard-sphere (VHS) collision model using an acceptance–rejection method (Bird 1994). The VHS model determines the likelihood of a collision based on the relative velocity and position of the two molecules under consideration. If a collision is determined to occur, the post-collision velocities are chosen at random from a Maxwellian velocity distribution function based on the relative velocity of the collision partners. The number of collision pairs chosen during each time step is based on the local collision frequency. To ensure a statistically representative sample, approximately 100 particles are placed initially in each cell. (The average number of particles per cell is 100. The actual number in each cell is based on the local number density.) The ratio of real to simulated molecules, $f_{num}$, for each simulation depends on $Kn$, with $f_{num}$ decreasing with increase in $Kn$. The time step, $\Delta t_{DSMC}$, is taken to be less than the mean collision time and the length of time it would take a molecule travelling at the most probable thermal velocity, $v_{mp} = 1065\,\mathrm{m\,s^{-1}}$ at 273.15 K, to cross a cell. In all cases, the latter constraint dictated the size of the time step, and for all the calculations presented in this study, we used $\Delta t_{DSMC} = 2.5 \times 10^{-10}$ s.

Collisions with the walls are assumed to be diffuse reflections with momentum and thermal accommodation coefficients, $\phi$, equal to unity. The computational boundaries in the $x$- and $y$-directions are treated as periodic. A total of $1 \times 10^4$ independent ensembles are performed. In these test problems, the flows are nominally one-dimensional, so we also average over the particle velocities in all nine cells at each $z$ position. Thus, since there are on average 100 particles in each cell at any given time, approximately $9 \times 10^6$ total velocity samples are used to obtain continuum-level quantities with low variances. Properties of the helium molecules and the VHS collision model are listed in table 1.

#### 2.3.1. *Navier–Stokes solution algorithm*

We solve the Navier–Stokes equations using the LCPFCT algorithm, which solves the coupled continuity equations for density, momentum and energy (Oran & Boris 2001). The computational domain is discretized into a set of finite volumes, and the conserved quantities ($\rho$, $\rho u$, $\rho v$, $\rho w$ and $\rho e$) are advanced forward in time at the cell centres using an explicit multistep time-advancement procedure. In the first step, the divergence of $\boldsymbol{\tau}$, the divergence of $\boldsymbol{q}$ and the dissipation function $\nabla\cdot(\boldsymbol{\tau}\cdot\boldsymbol{u}_0)$ are used to partially advance the solutions forward $\Delta t_{FV}$. Here, $\boldsymbol{\tau}$ and $\boldsymbol{q}$ are calculated according to the Navier–Newton viscosity model and Fourier's heat conduction model, respectively, using a second-order central finite-difference stencil. The viscosity and

| | | |
|---|---|---|
| $m_w$ (kg) | $6.65 \times 10^{-27}$ | Molecular weight |
| $T_r$ (K) | 273.15 | Reference temperature |
| $\omega$ | 0.66 | Viscosity–temperature power law exponent |
| $\sigma$ (m) | $2.33 \times 10^{-10}$ | Collision cross-section diameter |
| $\phi$ | 1.0 | DSMC wall accommodation coefficient |
| $\gamma$ | 1.66 | Specific heat ratio |
| $\mu_0$ (Pa s) | $1.865 \times 10^{-5}$ | Reference viscosity coefficient |
| $Pr$ | 0.72 | Prandtl number |
| $k_0$ (W m$^{-1}$ K$^{-1}$) | 0.1353 | Reference thermal conductivity |
| $R$ (J kg$^{-1}$ K$^{-1}$) | $2.07689 \times 10^3$ | Specific gas constant |
| $\phi_m$ | 1.0 | Navier–Stokes wall momentum accommodation coefficient |
| $\phi_T$ | 1.0 | Navier–Stokes wall thermal accommodation coefficient |

TABLE 1. Physical properties and VHS collision model parameters for helium gas.

thermal conductivity coefficients vary with temperature according to

$$\mu = \mu_0 \left( \frac{T}{T_r} \right)^{\omega}, \tag{2.13}$$

$$k = k_0 \left( \frac{T}{T_r} \right)^{\omega}, \tag{2.14}$$

where $\mu_0$ and $k_0$ are the viscosity and thermal conductivity at the reference temperature $T_r$, and $\omega$ is the viscosity–temperature index. The values of these quantities for helium gas are listed in table 1. In the second step, the convective terms of (2.1)–(2.3) are calculated using the flux-corrected transport algorithm (Boris *et al.* 1993) and the conserved variables are updated.

Two different boundary conditions are used at the walls. The no-slip, isothermal conditions,

$$u = V, \quad v = w = 0, \quad T = T_1, \tag{2.15}$$

at $z = 0$, and

$$u = v = w = 0, \quad T = T_2, \tag{2.16}$$

at $z = 10^{-4}$ m, are independent of $Kn$, whereas the first-order velocity and temperature slip conditions,

$$\frac{T_s}{T_w} = \left[ 1 + \frac{5}{2\overline{\omega}} \left( \frac{2\pi}{RT} \right)^{1/2} \lambda \left( \frac{\partial u}{\partial x} - 2\frac{\partial v}{\partial z} \right) \right]_s \left[ 1 + \frac{15}{4\overline{\omega}} \left( \frac{2\pi}{RT} \right)^{1/2} \lambda \left( \frac{\partial u}{\partial x} - 2\frac{\partial v}{\partial z} \right) - \frac{15\pi}{4\overline{\omega}} \frac{\gamma}{(\gamma - 1)Pr} \frac{2 - \phi_T}{\phi_T} \left( \frac{\lambda}{T} \frac{\partial T}{\partial z} \right) \right]_s^{-1}, \tag{2.17}$$

$$u_s = u_w + \frac{15\pi}{2\overline{\omega}} \left[ \frac{2 - \phi_m}{\phi_m} \lambda \left( \frac{\partial u}{\partial z} + \frac{\partial v}{\partial x} \right) \right]_s + \frac{3}{2\overline{\omega}} \frac{\gamma}{(\gamma - 1)Pr} \left( (2\pi RT)^{1/2} \frac{\lambda}{T} \frac{\partial T}{\partial x} \right)_s, \tag{2.18}$$

$$\lambda = \frac{2}{15\overline{\omega}} \frac{\mu}{\rho (2\pi RT)^{1/2}}, \tag{2.19}$$

$$\overline{\omega} = (7 - 2\omega)(5 - 2\omega), \tag{2.20}$$

depend on the local mean free path of the gas molecules as well as $\omega$. The subscript '$s$' indicates a quantity evaluated at the slip plane a distance of $\lambda$ from the walls. Both

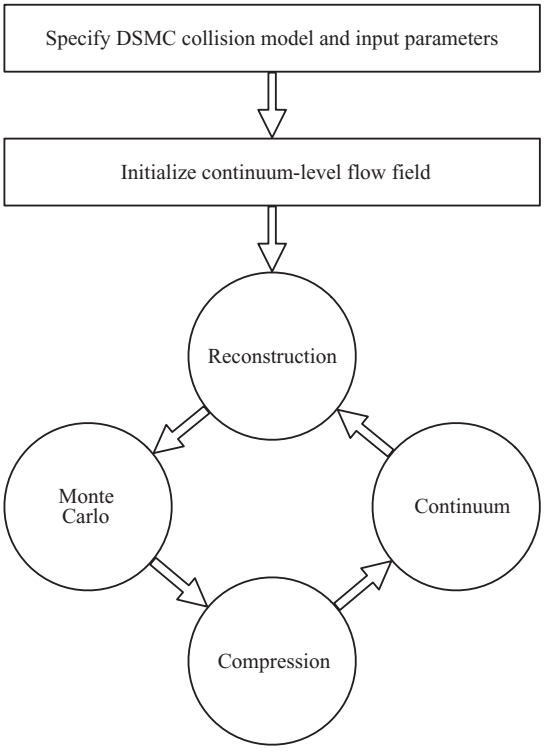


FIGURE 2. Schematic diagram of the CM$^3$.

the momentum and thermal accommodation coefficients, $\phi_m$ and $\phi_T$, are taken to be unity. The system is assumed to be periodic in the $x$- and $y$-directions.

### 2.4. *Multiscale solution algorithm (coupled multiscale, multiphysics method)*

We are concerned with finite-$Kn$ gas flows for which the Navier–Stokes equations fail to describe the molecular-level transport processes adequately. The Boltzmann equation is accurate over a much larger range of $Kn$, but it is inordinately more expensive to solve than the continuum-level conservation laws. Here we describe a method of simulating finite-$Kn$ flows that incorporates additional physics from the small-scale molecular motions into the continuum framework of (2.1)–(2.3). The CM$^3$ uses a Monte Carlo method to solve the Boltzmann equation at various instants in time and calculates $\boldsymbol{\tau}$ and $\boldsymbol{q}$ using (2.11)–(2.12) and the molecular velocities. The computed $\boldsymbol{\tau}$ and $\boldsymbol{q}$ are then substituted into (2.1)–(2.3), and these equations are advanced forward in time using a finite-volume method.

A depiction of the solution algorithm is shown in figure 2. After an initial continuum-level flow field is specified, the Monte Carlo continuum cycle, which is made up of four stages, begins. This Monte Carlo continuum cycle is repeated as necessary to provide updated instantaneous values for $\boldsymbol{\tau}$ and $\boldsymbol{q}$, so that the unsteady evolution of the flow is calculated correctly.

#### 2.4.1. *Stage 1: reconstruction*

In the first stage, we initialize the velocities of a set of particles so that the macroscopic flow variables are consistent with the current continuum-level flow

field. Velocity, density and temperature fields are interpolated to the centres of the DSMC cells (if different from those of the finite-volume grid). The number density of molecules (and hence the number of particles) is calculated from the mass density $\rho$ using the molecular weight of the constituent gas molecules. The velocity of each particle is randomly assigned from a prescribed velocity-distribution function (VDF) using an acceptance–rejection method (Bird 1994). The choice of the initial distribution is arbitrary, and in the results that follow, two different initial distributions will be considered: the equilibrium or Maxwellian distribution,

$$f_0(\boldsymbol{c}') = \left(\frac{m_w}{2\pi k_b T}\right)^{3/2} \exp\left(\frac{-m_w c'^2}{2k_b T}\right), \tag{2.21}$$

where $k_b$ is the Boltzmann constant, and the Chapman–Enskog distribution,

$$f_{CE}(\boldsymbol{c}') = f_0(\boldsymbol{c}')\left[1 + \left(\frac{m_w}{Pk_b T}\right)\left(\left(\frac{m_w}{2Pk_b T}\right)\frac{2c'^2}{5} - 1\right)(q_1 u' + q_2 v' + q_3 w')\right.$$
$$\left. - \frac{m_w}{Pk_b T}(\tau_{12}u'v' + \tau_{13}u'w' + \tau_{23}v'w') - \frac{m_w}{2PK_b T}(\tau_{11}(u'^2 - w'^2) + \tau_{22}(v'^2 - w'^2))\right]. \tag{2.22}$$

2.4.2. *Stage 2: Monte Carlo*

The purpose of the Monte Carlo stage of the cycle is to obtain accurate estimates of the instantaneous $\boldsymbol{\tau}$ and $\boldsymbol{q}$ for the local flow conditions. To do so, we obtain an approximation of the true velocity distribution by an iterative process in which a sequence of $f_i$ is generated by solving Boltzmann's equation over a finite time interval $M\Delta t_{DSMC}$ using $f_{i-1}$ and the local continuum flow variables as the initial conditions for each iteration. As the number of iterations grows, the sequence converges to $f$. This 'maturation' process is similar to that used by Al-Mohssen *et al.* (2007). If the particle velocities are initialized using (2.21), $\boldsymbol{\tau}$ and $\boldsymbol{q}$ are initially zero. If the particle velocities are taken from $f_{CE}$, $\boldsymbol{\tau}$ and $\boldsymbol{q}$ are initially equal to the Navier–Stokes stresses and heat fluxes. In non-equilibrium (high-$Kn$) flows, the true $\boldsymbol{\tau}$ and $\boldsymbol{q}$ are different from these initial values, and a finite number of iterations, $N_{MC}$, are needed to achieve convergence.

The Monte Carlo algorithm used here to solve the Boltzmann equation is a slight variation of the standard DSMC algorithm (Bird 1994). The process begins by initializing the DSMC particle velocities from either a Maxwellian or a Chapman–Enskog velocity-distribution function whose shape is based on $\boldsymbol{u}_0$ and $T$, and, if using $f_{CE}$, the continuum-level $\boldsymbol{\tau}$ and $\boldsymbol{q}$ are approximated using the Navier–Newton and Fourier models with $\mu_0$ and $\kappa_0$ from table 1. The typical DSMC move and collide processes are performed for a short period of time, $M\Delta t_{DSMC}$. Molecular collisions are calculated using the VHS collision model. Particle interactions with the walls are taken to be diffuse reflections with full thermal and momentum accommodation. The $x$- and $y$-boundaries are assumed to be periodic. At the end of this interval, the particle velocities, which are now described by a new distribution function $f_i$, are shifted and scaled so that the continuum-level velocity, temperature and density in each cell are equal to their initial values. The procedure is to sample the instantaneous particle velocities every $m$ time steps (with $m < M$). Since $M$ is taken to be small, we assume that the system is ergodic over this short time interval and calculate time averages over the $M/m$ samples to obtain an average velocity and temperature in each cell at

time $t_0 + M\Delta t_{DSMC}$, according to

$$N_s = \sum_{j=1}^{M/m} (N_a)_j, \tag{2.23}$$

$$\overline{\boldsymbol{u}}^* = \frac{1}{N_s} \sum_{j=1}^{M/m} \sum_{i=1}^{N_{aj}} \boldsymbol{c}_i, \tag{2.24}$$

$$\overline{T}^* = \frac{m_w}{3k_b} \left[ \frac{1}{N_s} \sum_{j=1}^{M/m} \sum_{i=1}^{N_{aj}} c_i^2 - \overline{u}^{*2} \right], \tag{2.25}$$

where $N_{aj}$ is the number of particles in a given cell at the $j$th sample. The necessary velocity shift $\delta\boldsymbol{u}$ and temperature scale $\alpha$ are then calculated from

$$\delta\boldsymbol{u} = \overline{\boldsymbol{u}}^* - \boldsymbol{u}_o, \tag{2.26}$$

$$\alpha = \sqrt{\frac{T_o}{\overline{T}^*}}. \tag{2.27}$$

Finally, the new particle velocities are calculated by subtracting $\delta\boldsymbol{u}$ from each particle in the cell and scaling the result by $\alpha$, i.e.

$$\boldsymbol{c}_i^* = \alpha(\boldsymbol{c}_i - \delta\boldsymbol{u}). \tag{2.28}$$

The number density in each cell is conserved by either adding or removing particles from the system. When particles must be added to a cell, i.e. $n^{t+M\Delta t_{DSMC}} < n^t$, their new velocities are set equal to those of randomly chosen particles within that cell. The positions of the particles are randomly chosen within the cell. The total number of particles in the simulation is conserved. That is, the sum of the number of particles removed from the entire domain during each rescaling event, $N_{rem}$, is equal to the number of particles added to the entire domain, $N_{add}$.

The resulting distribution of particle velocities, $f_1$, with $\overline{\boldsymbol{u}} = \boldsymbol{u}_0$ and $\overline{T} = T_0$, is used as the initial condition for a new Monte Carlo simulation. The process continues until the sequence of $f_i$ is sufficiently converged that $\boldsymbol{\tau}_{i+1} \approx \boldsymbol{\tau}_i$ and $\boldsymbol{q}_{i+1} \approx \boldsymbol{q}_i$.

### 2.4.3. *Stage 3: compression*

In the compression phase, we calculate $\boldsymbol{\tau}$ and $\boldsymbol{q}$ from the molecular-level velocities and condition the data so that they are suitable to use with the finite-volume solver in the final stage. This is done in two separate steps. In the first step, noise caused by statistical fluctuations in the sampled molecular velocities is reduced to levels below a threshold value. In the second step, smooth fields for the approximated $\boldsymbol{\tau}$ and $\boldsymbol{q}$ are constructed from the stochastic representation.

By design, DSMC gives a statistical representation of the flow properties, the variance of which depends on the number of independent samples used to calculate average quantities. For unsteady flows, a large number of independent ensembles are calculated to increase the number of samples. For the one-dimensional test problems presented in this study, we used $9 \times 10^5$ total velocity samples, where the total number of samples is equal to the product of the average number of particles in any cell, the nine cells at each $z$-location, and the number of independent ensembles performed during the Monte Carlo stage, to calculate the averages in (2.11)–(2.12). This number of samples was sufficient to reduce the statistical fluctuations in $\boldsymbol{\tau}$ and $\boldsymbol{q}$ to a

manageable level for the test cases. Some flows, particularly dense, low-velocity flows, require more sophisticated variance-reduction methods, such as nonlinear filtering (Kaplan & Oran 2002), low-variance DSMC (LVDSMC) (Baker & Hadjiconstantinou 2005; Homolle & Hadjiconstantinou 2007), a 'ghost-particle' method (Chun & Koch 2005), a molecular block method using artificially massive particles (Pan, Ng & Lam 2001) or the information-preservation (IP) method (Fan & Shen 2001; Sun & Boyd 2002). While such methods were not necessary for the flows considered here, they may be used for different flow configurations.

The next step is to condition the averaged values of $\boldsymbol{\tau}$ and $\boldsymbol{q}$ for use with a continuum-level finite-volume solver. By conditioning, we mean constructing a continuous field from stochastic data. This is necessary to compute the divergence of these quantities in (2.1)–(2.3). We use one-dimensional cubic B-splines (Dierckx 1975, 1982, 1993) to fit a smooth curve to the data. The smoothness of the curve can be controlled by a smoothness factor $f_s$. Large values of $f_s$ produce curves devoid of localized fluctuations, but tend to smooth out real variations in $\boldsymbol{\tau}$ and $\boldsymbol{q}$. Conversely, small values of $f_s$ will capture the physical variations but will be too noisy to use for calculating the divergence of these variables. Here, separate values of $f_s$ for $\boldsymbol{\tau}$ and $\boldsymbol{q}$ are chosen empirically for each test problem to limit the amount of noise yet retain continuum-level variations.

### 2.4.4. *Stage 4: solving continuum-level equations*

Finally, the continuum-level variables are advanced forward in time $\delta t_{FV}$ using the general conservation equations (2.1)–(2.3) and the spatial representations of $\boldsymbol{\tau}$ and $\boldsymbol{q}$ computed in the previous stage. The computational domain is discretized into a set of finite volumes, and the conserved quantities ($\rho$, $\rho u$, $\rho v$, $\rho w$ and $\rho e$) are advanced forward in time at the cell centres using an explicit multistep time-advancement procedure. The local time step for the finite-volume solver, $\Delta t_{FV}$, is chosen in the standard way to ensure numerical stability. In the first step, the divergence of $\boldsymbol{\tau}$, the divergence of $\boldsymbol{q}$ and the dissipation function $\nabla\cdot(\boldsymbol{\tau}\cdot\boldsymbol{u}_0)$ are used to partially advance the solutions forward $\Delta t_{FV}$. Standard second-order central finite-difference stencils are used to perform the numerical differentiation. In the second step, the convective terms of (2.1)–(2.3) are calculated using the flux-corrected transport algorithm (Boris *et al.* 1993; Oran & Boris 2001), and the conserved variables are updated. The simple isothermal, no-slip boundary conditions (see (2.15)–(2.16)) are used at the wall boundaries, and periodic boundary conditions are applied in the $x$- and $y$-directions. The time advancement continues for $\delta t_{FV}$ using the same closure data for $\boldsymbol{\tau}$ and $\boldsymbol{q}$. At the end of the integration cycle, the updated continuum-level variables are sent to stage 1 and the cycle is repeated.

Two primary issues arise when developing a multiscale algorithm for finite-$Kn$ gas flows: how to calculate accurate continuum-level representations of molecular-level stresses and energy fluxes, and how to couple this molecular-level information to an unsteady solution algorithm for the general conservation equations. As with any other computational algorithm, there are several parameters that must be specified based on the physics of the flow being computed: the number of time steps between rescaling events, $M$, and the number of time steps between samples for the rescaling, $m$; the choice of the initial velocity-distribution function used in the reconstruction stage, the 'maturation' time for $\boldsymbol{\tau}$ and $\boldsymbol{q}$, $\delta t_{DSMC} = N_{MC}(M\Delta t_{DSMC})$; the number of independent ensembles needed to collect a sufficiently large velocity sample, the smoothing factor $f_s$ for the spatial field construction of $\boldsymbol{\tau}$ and $\boldsymbol{q}$; and the size of each continuum-level time advancement period, $\delta t_{FV}$. In the following sections, we address these issues and discuss how proper values for the control parameters can be determined by using the

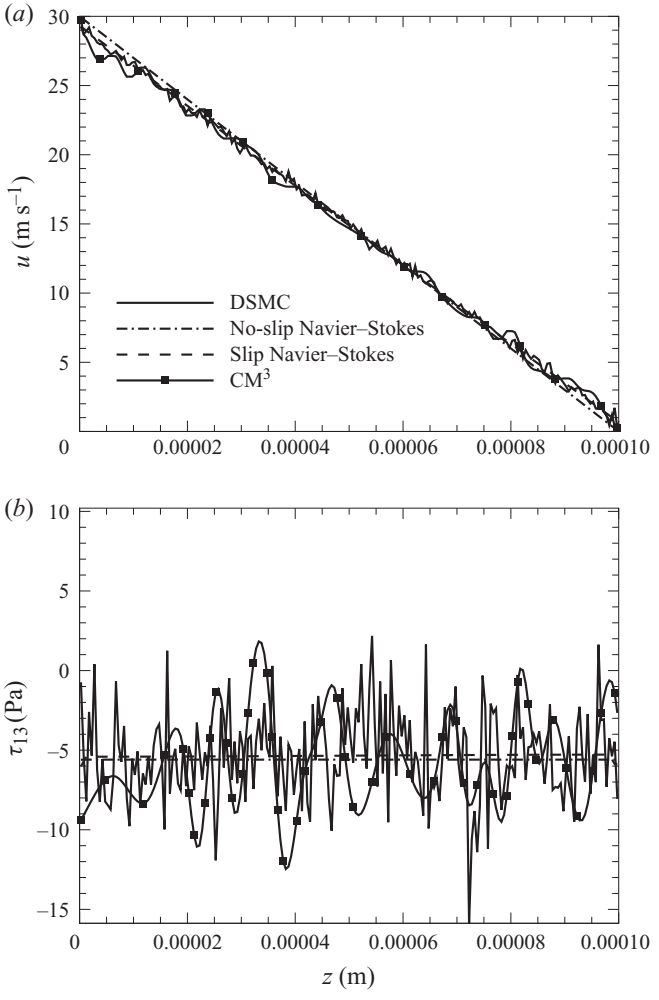


FIGURE 3. Steady-state (*a*) velocity and (*b*) shear-stress profiles for Rayleigh flow with $Kn = 0.02$ calculated using DSMC, no-slip (see (2.15)–(2.16)) and slip (see (2.17)–(2.18)) Navier–Stokes equations, and $CM^3$.

multiscale method to solve two canonical flows: an isothermal, low-Mach-number Rayleigh flow (unsteady Couette flow) and a quiescent Fourier flow.

## 3. Results

### 3.1. *One-dimensional low-Ma Rayleigh flow*

In the first test problem, the temperatures of the two plates are held constant at 273.15 K, and the bottom plate is set in motion with velocity $V = 30\,\mathrm{m\,s^{-1}}$. The Mach number based on this ambient temperature and the velocity of the moving plate is $Ma = 0.03$. Accordingly, viscous dissipation will be negligible, and the temperature throughout the flow will remain nearly constant. For this one-dimensional flow, the only non-zero component of the stress tensor is the deviatoric stress $\tau_{13}$.

Figures 3–5 show the steady-state $u$ and $\tau_{13}$ profiles calculated using the Navier–Stokes equations with no-slip and slip boundary conditions, DSMC and the $CM^3$ for $Kn = 0.02$, 0.2 and 1, respectively. The control parameters for the multiscale

| Parameter | $Kn = 0.02$ (figure 3) | $Kn = 0.2$ (figure 4) | $Kn = 1$ (figure 5) |
|---|---|---|---|
| $N_{MC}$ | 20 | 60 | 60 |
| $M$ | 5 | 5 | 5 |
| $m$ | 1 | 1 | 1 |
| $f_s$ | 5 | 100 | $1.0 \times 10^4$ |
| $\delta t_{FV} / \Delta t_{DSMC}$ | 20 | 20 | 20 |

TABLE 2. Multiscale control parameters used to calculate the Rayleigh flow (figures 3–5).

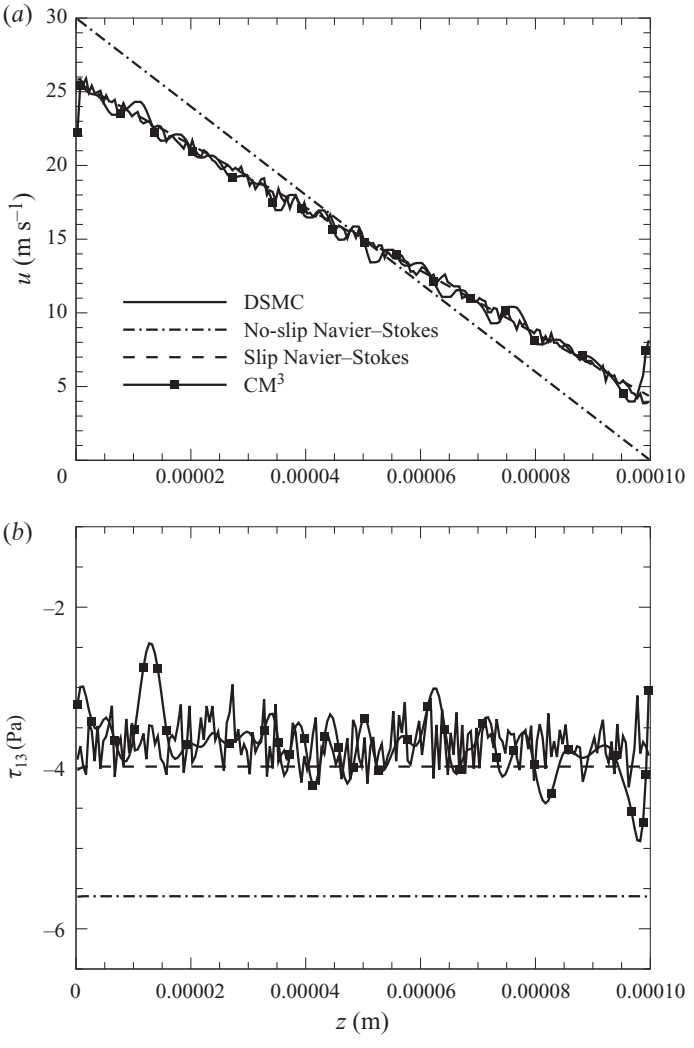


FIGURE 4. Steady-state ($a$) velocity and ($b$) shear-stress profiles for Rayleigh flow with $Kn = 0.2$ calculated using DSMC, no-slip (see (2.15)–(2.16)) and slip (see (2.17)–(2.18)) Navier–Stokes equations, and CM$^3$.

algorithm used in each example are given in table 2. The procedure for determining these values will be discussed in detail in the following section. While the Navier–Stokes equations are an acceptable model for small $Kn$, we do not expect them,

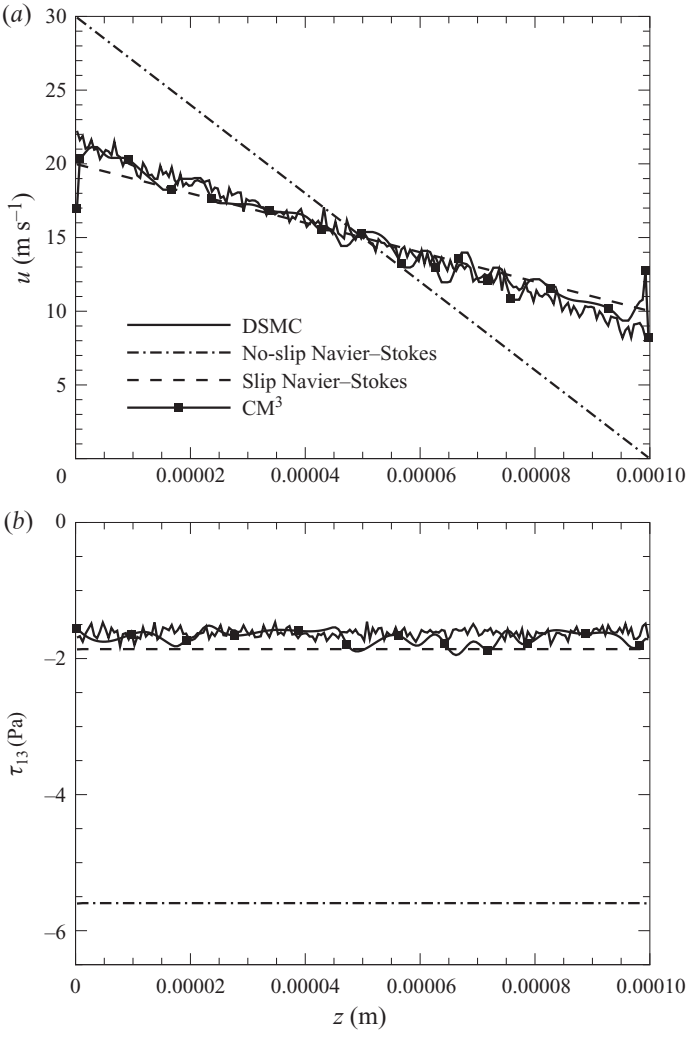


FIGURE 5. Steady-state (*a*) velocity and (*b*) shear-stress profiles for Rayleigh flow with $Kn = 1$ calculated using DSMC, no-slip (see (2.15)–(2.16)) and slip (see (2.17)–(2.18)) Navier–Stokes equations, and CM$^3$.

even with slip boundary conditions, to be accurate when $Kn$ is large. Higher-order continuum models (e.g. the Burnett equations) would give more accurate solutions. We include these solutions to show that DSMC solutions converge to the continuum solutions for small $Kn$. We do not claim that the multiscale solutions are more accurate than the Navier–Stokes equations since they are being applied outside of their range of applicability. The accuracy of the multiscale solutions is judged by comparing them with the corresponding DSMC solutions, which we take to be exact solutions of the Boltzmann equation.

For $Kn = 0.02$ (figure 3), the DSMC solution is comparable to the Navier–Stokes solution with no-slip boundary conditions and matches well the solution calculated using the first-order slip boundary conditions. The velocity slip is just less than 1 m s$^{-1}$ at the walls, and the CM$^3$ solution also reproduces this. For $Kn = 0.2$ (figure 4), the velocity slip increases to about 4.5 m s$^{-1}$. The Navier–Stokes equations with slip

| Parameter | $Kn = 0.02$ (figure 6) | $Kn = 0.2$ (figure 7) | $Kn = 1$ (figure 8) |
|---|---|---|---|
| $N_{MC}$ | 60 | 200 | 400 |
| $M$ | 5 | 5 | 5 |
| $m$ | 1 | 1 | 1 |
| $f_s$ | $1.0 \times 10^{10}$ | $1.5 \times 10^{8}$ | $1.1 \times 10^{6}$ |
| $\delta t_{FV} / \Delta t_{DSMC}$ | 10 | 10 | 10 |

TABLE 3. Multiscale control parameters used to calculate the Fourier flow (figures 6–8).

boundary conditions still do a reasonable job of predicting the velocity profile for this value of $Kn$. The multiscale solution for this case also matches the DSMC solution quite well. For $Kn = 1$, the flow is considerably more rarefied, and the Navier–Stokes solutions, even with velocity slip boundary conditions, no longer correctly describe the flow. The DSMC solution shows a large velocity slip of $8\,\mathrm{m\,s^{-1}}$ ($\approx 27\,\%$ of the wall velocity). The multiscale solution accurately reproduces the DSMC solution everywhere except in very narrow regions (approximately two cells wide) near the walls. Here, complications arise due to the simple boundary conditions used in the multiscale algorithm. A more detailed analysis of the wall boundary conditions is left for future work. In all three examples, we performed enough ensemble averaging during the calculation of the multiscale solutions to ensure that spatial variations in the approximate $\tau_{13}$ profiles were similar to those in the standard DSMC solutions. As with any DSMC calculation, increasing the number of sampling events during the Monte Carlo stage of the CM$^3$ will decrease the magnitude of these spatial fluctuations.

### 3.2. *Fourier flow*

We next consider a stationary Fourier flow (i.e. $V = 0$) in which the temperature of the bottom plate is $T_1 = 293.15\,\mathrm{K}$ and that of the top plate is $T_2 = 253.15\,\mathrm{K}$. As in the previous section, three different average values of $Kn$ are examined: $Kn = 0.02$, 0.2 and 1. In each case, $Kn$ varies with temperature from a maximum at the bottom plate, approximately 5 % larger than the average value, to a minimum at the top plate, approximately 5 % smaller than the average value.

In the continuum limit, the solution to the Navier–Stokes equations for this particular flow using no-slip, isothermal boundary conditions is

$$T_{NS} = T_1 \times \left[ \left( \left( \frac{T_2}{T_1} \right)^{\omega+1} - 1 \right) z + 1 \right]^{1/(\omega+1)}, \tag{3.1}$$

$$q_{3_{NS}} = \frac{\kappa_0}{T_0^{\omega} h} \frac{T_2/T_1 - 1}{\omega + 1} T_1^{\omega+1}. \tag{3.2}$$

A closed-form, analytical solution does not exist for finite $Kn$ using the slip boundary condition (2.17), and the governing equations must be solved numerically. We compare the no-slip and slip Navier–Stokes solutions to results obtained using DSMC and CM$^3$ for $Kn = 0.02$, 0.2 and 1. Steady-state profiles of temperature and wall-normal heat flux $q_3$ for each of these values of $Kn$ are shown in figures 6–8, respectively. The control parameters for the multiscale algorithm used in each case are listed in table 3.

Again, for small $Kn = 0.02$, the Navier–Stokes solution with slip boundary conditions agrees well with the DSMC solution. The temperature slip at the walls of only 1.5 K is found using all three models. The DSMC results obtained for

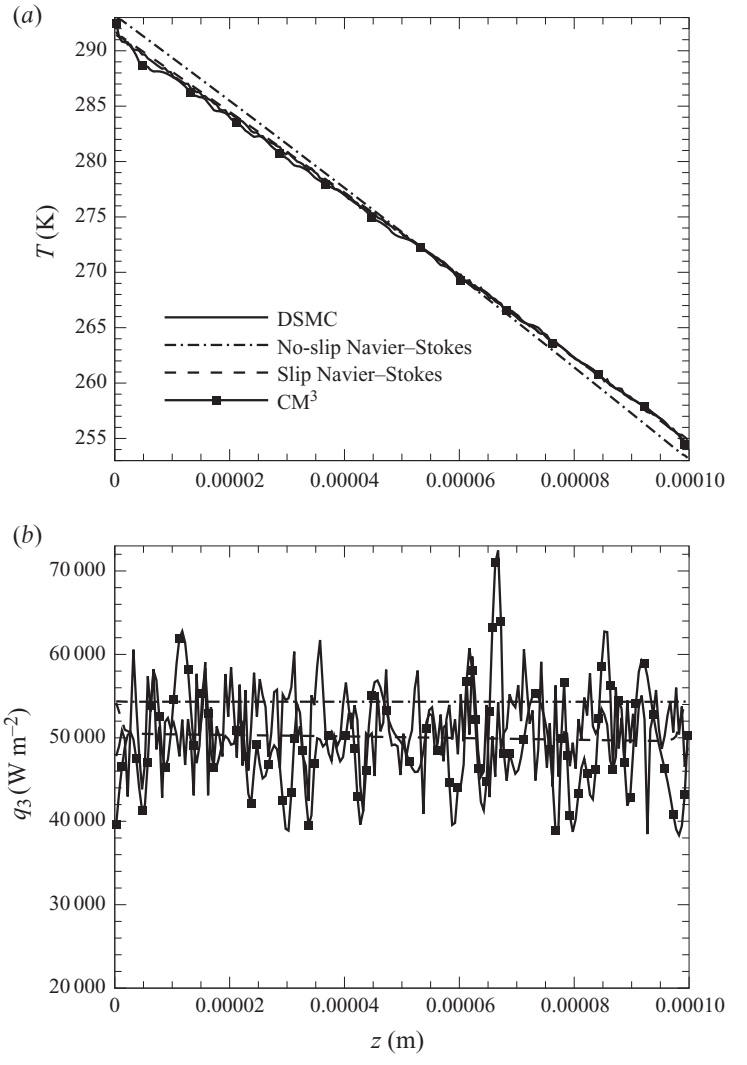


FIGURE 6. Steady-state (*a*) temperature and (*b*) wall-normal heat-flux profiles for Fourier flow with $Kn = 0.02$, $T_2 = 253.15\,\mathrm{K}$ and $T_1 = 293.15\,\mathrm{K}$ calculated using DSMC, no-slip (see (2.15)–(2.16)) and slip (see (2.17)–(2.18)) Navier–Stokes equations, and $\mathrm{CM}^3$.

$Kn = 0.2$ (figure 7) show that the temperature profile becomes nonlinear at this level of rarefaction. The Navier–Stokes solutions do not exhibit the same degree of nonlinearity, but the temperature-slip profile does reasonably well at predicting the correct solution away from the walls, suggesting that $Kn = 0.2$ is close to the breakdown limit for the Navier–Stokes equations. The $\mathrm{CM}^3$ does correctly predict the nonlinearity in the temperature profile and agrees with the DSMC temperature over the entire flow field. The flow is sufficiently rarefied for $Kn = 1$ (figure 8) that the Navier–Stokes equations no longer hold, and significant differences between the Navier–Stokes slip solution and the DSMC solution are found in both the temperature and heat-flux profiles. The multiscale algorithm, however, once again gives a good approximation to the DSMC solution.

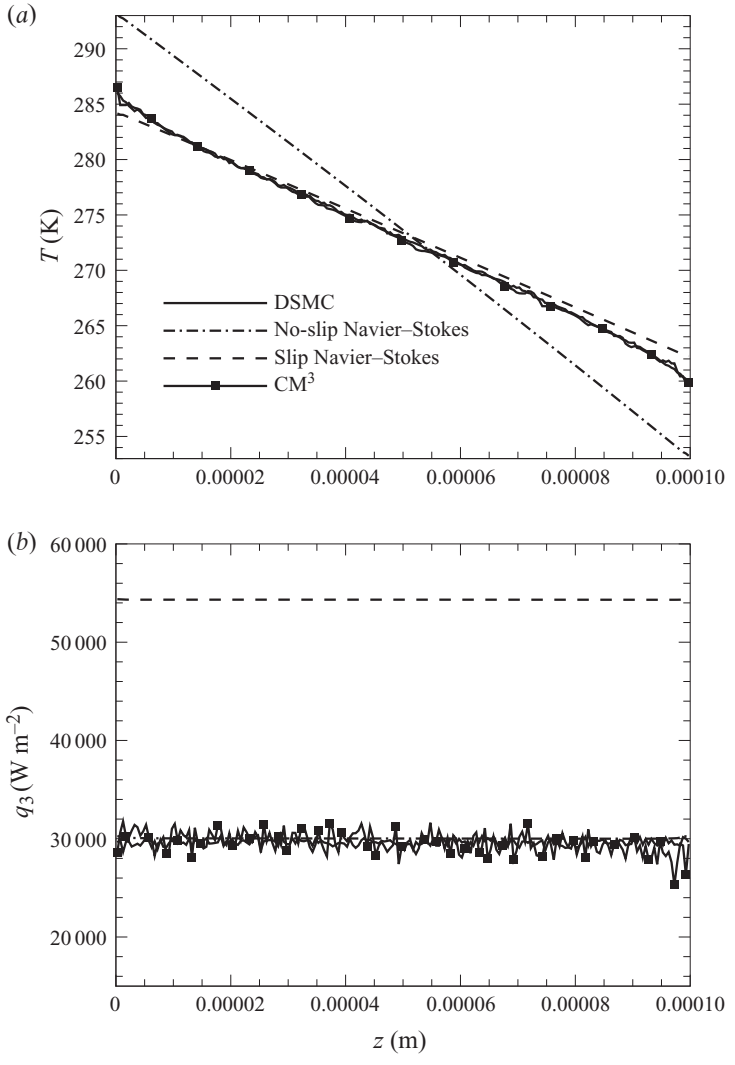


FIGURE 7. Steady-state (*a*) temperature and (*b*) wall-normal heat-flux profiles for Fourier flow with $Kn = 0.2$, $T_2 = 253.15\,\mathrm{K}$ and $T_1 = 293.15\,\mathrm{K}$ calculated using DSMC, no-slip (see (2.15)–(2.16)) and slip (see (2.17)–(2.18)) Navier–Stokes equations, and CM$^3$.

## 4. Discussion

### 4.1. *Calculation of* $\boldsymbol{\tau}$ *and* $\boldsymbol{q}$

The most critical step in the multiscale algorithm is calculating $\boldsymbol{\tau}$ and $\boldsymbol{q}$ accurately using the molecular-level model. The approach we take here is to allow an arbitrary distribution of molecular velocities to mature to a distribution representative of a real collection of molecules with specified $\boldsymbol{u}$, $T$ and $\rho$ through simulated molecular collisions. This procedure gives a series of successively more accurate approximations, $f_0,\ f_1,\ f_2, \ldots, f_N$, to the distribution function $f$. There are three issues that must be addressed: the choice of initial distribution function $f_0$, the details of the particle velocity shifting and scaling process, and the total length of time required for maturation or, equivalently, the number of successive approximations that need

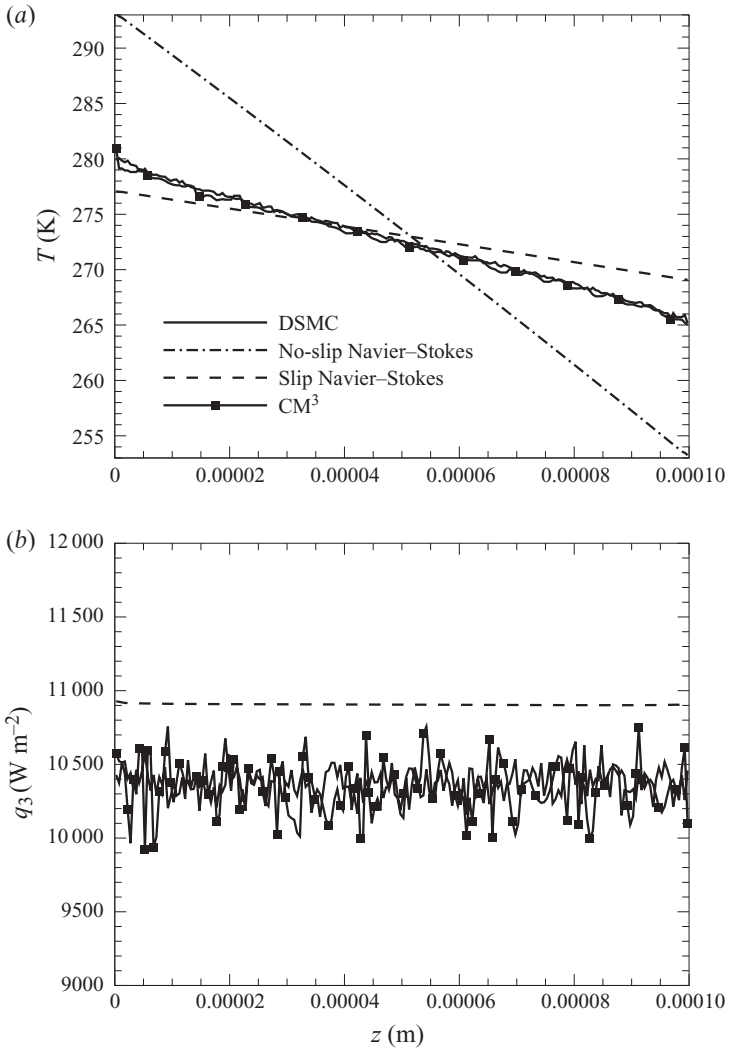


FIGURE 8. Steady-state (*a*) temperature and (*b*) wall-normal heat-flux profiles for Fourier flow with $Kn = 1$, $T_2 = 253.15\,\mathrm{K}$ and $T_1 = 293.15\,\mathrm{K}$ calculated using DSMC, no-slip (see (2.15)–(2.16)) and slip (see (2.17)–(2.18)) Navier–Stokes equations, and CM$^3$.

to be generated by solving the constrained Boltzmann equation before a mature distribution is reached.

In the reconstruction phase of each cycle in the multiscale method, initial velocities are assigned to a set of DSMC particles. The only restrictions are that $\boldsymbol{u}$ and $T$ in each cell are equal to specified values. The choice of distribution function that satisfies this constraint is not unique. For instance, the two most commonly used distribution functions, the Maxwellian (i.e. (2.21)) and the Chapman–Enskog (i.e. (2.22)), produce two different velocity distributions for the same first moments, $\boldsymbol{u}$ and $T$. Higher-order moments of these distributions (e.g. $\boldsymbol{\tau}$ and $\boldsymbol{q}$) differ substantially; however, both represent equally valid initial conditions for the Boltzmann equation. Figure 9 shows a representative higher-order moment of several different intermediate approximations of $f$ calculated using the Monte Carlo phase of the multiscale algorithm started by

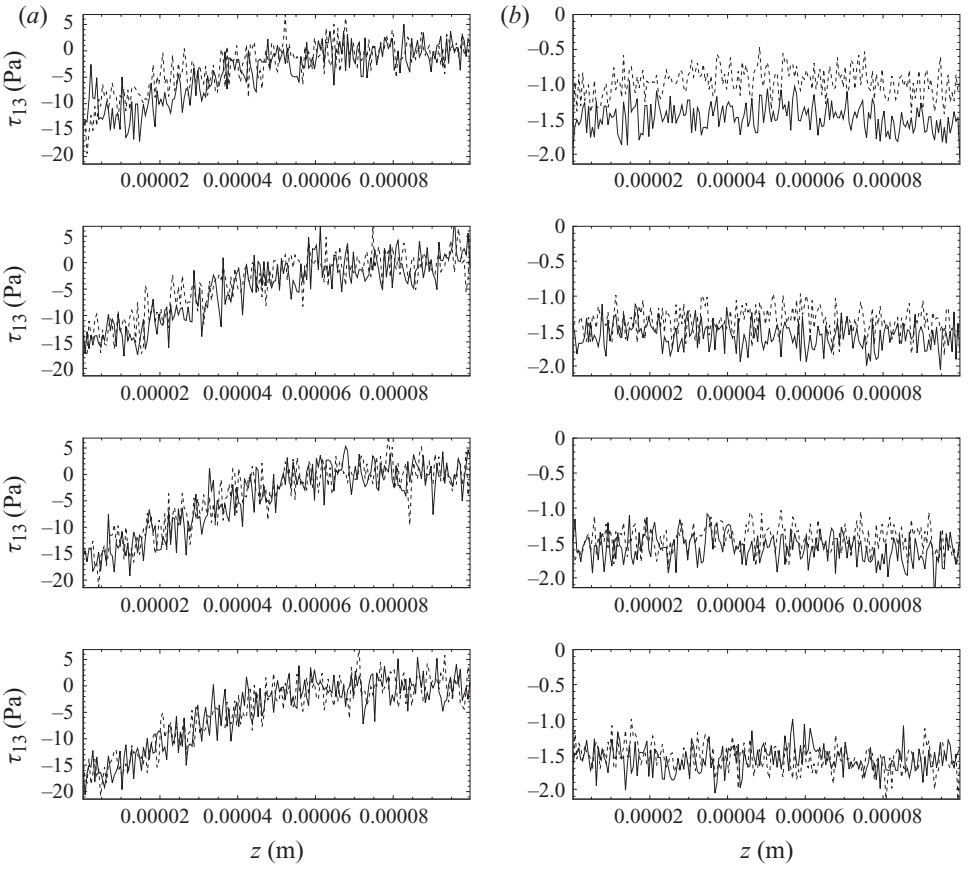


FIGURE 9. Sequence of $\tau_{13}$ profiles obtained for successively more accurate representations of $f$ generated via the Monte Carlo process starting from an intermediate continuum solution for (*a*) $Kn = 0.02$ and (*b*) $Kn = 1$. From top to bottom in (*a*), the curves represent the solutions after two, four, six and eight iterations of the Monte Carlo process. From top to bottom in (*b*), the curves represent solutions at 40, 80, 120 and 160 iterations. The solid lines are the solutions initialized from a Chapman–Enskog distribution and the dashed lines are those initialized from a Maxwellian distribution.

using a Maxwellian (dashed lines) and a Chapman–Enskog (solid lines) distribution function. The plot on the left (figure 9*a*) is for a small $Kn$ ($=0.02$), and the one on the right is for a large $Kn$ ($=1$). In both examples, the $\tau_{13}$ profiles converge to the same values regardless of the initial condition. The only difference is the number of iterations required to reach this final $\tau_{13}$. In the continuum limit (small $Kn$), $\boldsymbol{\tau}$ and $\boldsymbol{q}$ approach the Navier–Stokes solution, which is equivalent, by construction, to that obtained for the Chapman–Enskog distribution. For larger $Kn$, there is no general criterion as to which initial distribution the true higher-order moments will be closer. For the Rayleigh problems presented in the previous section, converged solutions were obtained more quickly when starting from a Chapman–Enskog distribution function for $Kn = 1$, whereas using a Maxwellian as the initial distribution offered a slight advantage for the Fourier flow at the same level of rarefaction. Ideally, we would like to construct a better approximation of the true velocity distribution to use as an initial condition, particularly for large $Kn$.

If left unchecked during the maturation period, the average velocity, temperature and density in each cell would drift from their initial values if the flow is not in a steady state. This would prevent the higher-order moments from reaching their matured values. To keep this from happening, we shift and scale the molecular velocities every $M$ time steps (cf. § 2.4.2). This procedure regulates the bulk velocity and acts as a thermostat for average temperature. The choice of the parameter $M$ is set to keep $\rho \boldsymbol{u}^{t+M\Delta t} \approx \rho \boldsymbol{u}^{t}$, while ensuring that enough samples of molecular velocities can be collected in that interval to calculate $\rho \boldsymbol{u}^{t+M\Delta t}$. The rate of change of the macroscopic variables can be estimated from the Navier–Stokes equations by considering the magnitude of the largest component of the stress tensor or heat-flux vector. For the Rayleigh flow, a steep gradient in $\tau_{13}$ of $\approx 1 \times 10^{7}\ \mathrm{Pa\,m^{-1}}$ develops during the initial acceleration of the flow after the top plate is set in motion. Using $\Delta t_{DSMC} = 2.5 \times 10^{-10}$ s, the magnitude of the corresponding change in linear momentum ($\Delta \rho u$) during one time step is $2.5 \times 10^{-3}\ \mathrm{Pa\ s\,m^{-1}}$. In the Fourier flow, the magnitude of the change in internal energy during one time step ($\Delta \rho e$) was larger ($\approx 0.1\ \mathrm{J\,m^{-3}}$). We want $\Delta \rho u$ and $\Delta \rho e \ll 1$; so $M$ is chosen to be as small as possible to provide enough samples to compute the average values with sufficiently low statistical variances. (Recall that velocity samples are taken every $m$ steps, so that the total number of velocity samples is of the order of $N_a(M/m)$.) In the example above, the molecular velocities were rescaled every five time steps based on velocities sampled every time step in that interval, i.e. $M = 5$ and $m = 1$. As will be discussed below, the average number of particles per cell, $N_a$, used in the calculations was a function of $Kn$, and some of the calculations had significantly larger numbers of particles and, hence, samples during the $M$ time steps.

For simple hard-sphere molecules ($\omega = 1/2$, $\alpha = 1$), the total number of molecular collisions per unit volume per unit time is

$$N_c = \sqrt{8\pi} d^2 n^2 \sqrt{2 k_b T / m_w}. \tag{4.1}$$

This value varies quadratically with the local number density, and hence, is a strong function of $Kn$. In the test problems considered in § 3, $N_c = 1.24 \times 10^{33}$, $1.24 \times 10^{31}$ and $4.98 \times 10^{29}\ \mathrm{m^{-3}\ s^{-1}}$ for $Kn = 0.02$, 0.2 and 1, respectively. In the Monte Carlo simulations, where the ratio of real molecules to simulated particles is represented by $f_{num}$, the total number of simulated collisions per unit volume per unit time is $N_c / f_{num}$. Using $\Delta t_{DSMC} = 2.5 \times 10^{-10}$ s and $\Delta x = \Delta y = \Delta z = 5.0 \times 10^{-7}$ m, the number of simulated collisions in each cell every time step are $38875/f_{num_1}$, $389/f_{num_2}$ and $16/f_{num_3}$ for $Kn = 0.02$, 0.2 and 1, respectively. During the $M$ time steps, there should be a sufficient number of simulated collisions in each cell to ensure that the average temperatures are computed correctly. Here, we require at least $N^* = 30$ collisions in the $M\Delta t$ time interval. This provides a lower bound for the number of particles that are needed in each cell, $N_{min} = N^* n / (M N_c \Delta t_{DSMC})$, which corresponds to $N_{min} = 40$, 400 and 2000 for $Kn = 0.02$, 0.2 and 1, respectively. In the multiscale simulations, we used $N = N_{min}$ for all cases except $Kn = 0.02$, for which we used $N = 100$ to improve the sampling statistics for $\boldsymbol{\tau}$ and $\boldsymbol{q}$.

The number of Monte Carlo iterations ($N_{MC}$) needed to ensure that $f_{MC}$ has matured long enough that the sequence of moments, $\boldsymbol{\tau}$ and $\boldsymbol{q}$, converge to their proper values depends on $Kn$, the initial choice of distribution function and the details of the flow field. This makes it impossible to assign a universal value to $N_{MC}$ (or $\delta t_{DSMC}$). In general, the convergence of $\boldsymbol{q}$ is slower than $\boldsymbol{\tau}$, and longer maturation times must be used in flows where there are significant energy fluxes. Likewise, the degree of non-equilibrium of the flow determines how far the matured fluxes are

from the initial equilibrium values. For the Rayleigh flows, the $\tau_{13}$ profiles converge to matured values after 6, 20 and 60 iterations for $Kn = 0.02$, 0.2 and 1, respectively, when starting from a Chapman–Enskog distribution. The $q_3$ profiles calculated for the Fourier flows required 60, 160 and 360 iterations to fully mature for the same three values of $Kn$. As mentioned above, the convergence for $Kn = 1$ was found to be faster when starting from a Maxwellian distribution for the Fourier flow, and the value of $N_{MC}$ listed above is based on this starting condition. Slightly larger values of $N_{MC}$ than those listed above were used in each of the corresponding calculations presented in § 3. In future work, we will implement an adaptive procedure for choosing the value of $N_{MC}$ that would eliminate unnecessary computations by stopping the maturation process once $\boldsymbol{\tau}$ and $\boldsymbol{q}$ reached steady values during each cycle.

### 4.2. *Coupling stochastic data to continuum solver*

Once an accurate description of the molecular state has been attained, it is necessary to build continuous functional representations of the stresses and energy fluxes that approximate the fields in the general conservation laws. This entails extracting sufficiently smooth fields from the statistically noisy DSMC data and determining for how long these approximate representations remain valid.

Smooth fields are constructed using a two-part process. In the first part, we reduce the statistical fluctuations in the calculated moments to levels where the mean signal is discernible from the noise. Formally, we require the standard deviation of the quantity $Q$ under consideration to be less than the change in the mean value of $Q$, $\overline{Q}$, over some spatial interval $\Delta L$, i.e. $\sigma_Q < \Delta L(\partial \overline{Q}/\partial x)$ for $\Delta L \sim O(\Delta x)$ for all $x$ in the domain. Statistical noise reduction in DSMC calculations is generally attained by performing time, ensemble and spatial averages. Since we are concerned with the unsteady evolution of the flow field, we cannot average over time, but rely only on taking ensemble and spatial averages of the velocity samples. The standard deviation of the noise in the components of $\boldsymbol{\tau}$ and $\boldsymbol{q}$ decreases as the square root of the total number of samples. More sophisticated methods for noise reduction exist (cf. § 2.4.3) that could be used in conjunction with this method to more efficiently decrease the fluctuations, but the problems considered here are sufficiently simple that this 'brute force' averaging procedure is feasible. For the examples discussed in § 3, a total of $9 \times 10^5$ samples were sufficient to reduce the noise to the level indicated above.

The second part of the smoothing process is to construct an approximation of the mean field $\tilde{Q}(x)$ based on the values calculated from DSMC. The main requirement is that the first derivatives of $\tilde{Q}(x)$ are continuous so that the divergences in (2.1)–(2.3) can be calculated. In this paper, we use B-splines of order 3 to construct $\tilde{Q}(x)$, which then has continuous derivatives up to $\mathrm{d}^2/\mathrm{d}x^2(Q)$. As discussed in § 2.4.3, we can influence the shape of $\tilde{Q}(x)$ by specifying a factor $f_s$ to strike a balance between fidelity of fit and smoothness of the interpolating spline (additional noise reduction). The representation of the function at each point in the domain, $\tilde{Q}_i$, is determined by minimizing the discontinuity in the third derivative of piecewise polynomials (of degree 3) that connect each point in space $x_i$ with the constraint that $\sum_i [(w_i(\overline{Q}_i - \tilde{Q}_i))^2] \leqslant f_s/\sigma_Q^2$. The weights $w_i$ are chosen to be equal to the inverse of the standard deviation of the spatial fluctuations in the computed moments, $\sigma_Q$, and acceptable values of $f_s$ lie in the interval $\sigma_Q^2(N_x - \sqrt{2N_x},\ N_x + \sqrt{2N_x})$. The value of $\sigma_Q$ can be calculated from the standard deviation of the velocity fluctuations used to calculate the moment by $\sigma_Q = \sigma_{v'^n}/\sqrt{N_s}$, where the subscript $v'^n$ represents the product of $n$ fluctuating velocity components and $N_s$ is the total number of velocity samples used to calculate any one of the $\overline{Q}_i$. Figure 10 shows several B-spline approximations

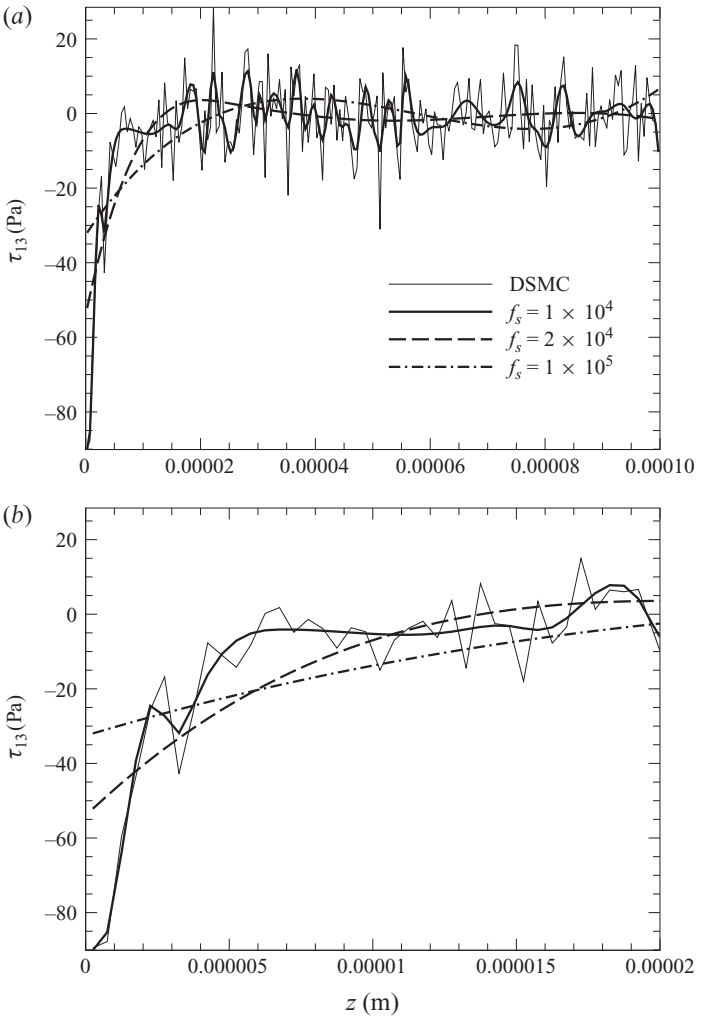


FIGURE 10. B-spline interpolations of the shear stress, $\tau_{13}$, at $t = 5\Delta t$ calculated using various values of $f_s$. Maturation of VDF using velocity shifting and scaling process for $\delta t_{DSMC} = 300\Delta t_{DSMC}$ with $M = 5$, $m = 1$. Low-speed Rayleigh flow ($V = 30\,\mathrm{m\,s^{-1}}$) at $Kn = 0.02$. (*a*) Complete profile and (*b*) close-up view of steep gradients near $z = 0$.

of a representative $\tau_{13}$ using various values of $f_s$ along with the original DSMC data. For this particular case, $f_s = 1 \times 10^4$ gives a curve that is reasonably smooth but still captures the steep gradient near $z = 0$. If inaccurate $\tilde{Q}(x)$ is used throughout the unsteady evolution, the steady-state solutions could differ from the exact (DSMC) solutions. As an example, figure 11 shows two steady-state velocity profiles calculated using the multiscale method with different $f_s$ for the Rayleigh flow and $Kn = 0.2$. Both CM$^3$ solutions compare well with the DSMC solution in the middle of the domain, but the solution for the larger $f_s$ is incorrect near the walls, where the gradients in $\tau_{13}$ are the steepest during the unsteady evolution of the flow field.

Once the simulated closure relations for the molecular-level stresses and heat fluxes have been constructed, it is necessary to decide how large a time step can be taken during the solution of the conservation equations, $\delta t_{FV}$. It is assumed that these

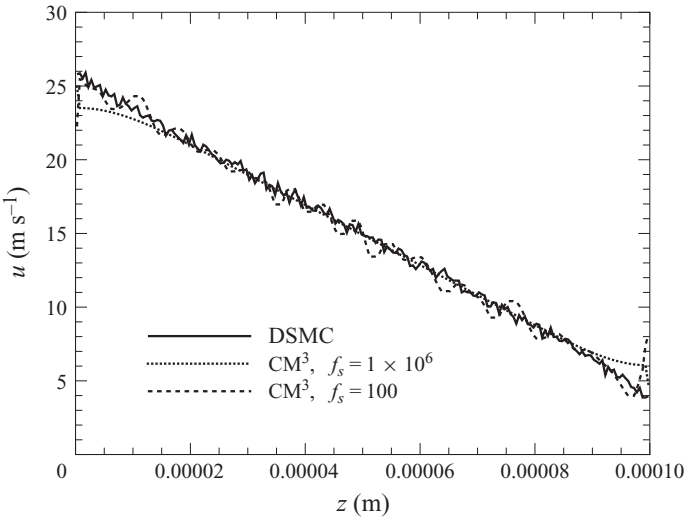


FIGURE 11. Steady-state velocity profile for Rayleigh flow with $Kn = 0.2$ calculated using DSMC, no-slip (see (2.15)–(2.16)) and slip (see (2.17)–(2.18)) Navier–Stokes equations, and CM$^3$. CM$^3$ profiles calculated using $f_s = 1 \times 10^6$ and $f_s = 100$.

modified balance equations lie on an invariant manifold in the state space, so that the projected solutions to these equations are reasonably accurate approximations to the conservation laws. Proof of this assumption is a complicated issue, particularly when $Kn \sim O(1)$, and is beyond the scope of this discussion. Recent work has, however, shown that closure relations for the linear hydrodynamic equations can be generated that do not use $Kn$ as a perturbation parameter, and so are equally valid for large $Kn$ (Gorban, Karlin & Zinovyev 2004). We assume that the closures used here for the nonlinear conservation laws are also independent of $Kn$, since they are generated naturally as quasi-equilibrium solutions of the Boltzmann equation. To the extent that these assumptions hold, we should be able to make a large advancement in time, relative to the time scale of the molecular motions, by using the closed conservation laws. In practice, the size of $\delta t_{FV}$ is limited by the rate of change of the macroscopic variables. For the Rayleigh flow, the streamwise momentum evolves according to

$$\frac{\partial \rho u}{\partial t} = \frac{\partial \tau_{13}}{\partial z}, \tag{4.2}$$

and it is a fairly simple procedure to estimate how quickly the momentum changes once an approximation for $\tau_{13}$ is obtained. For a more general flow, such a simplified description of the evolution does not exist, and one must turn to other methods to estimate the magnitude of the most rapidly varying conserved variable, $|\partial\phi/\partial t|$. One possibility is to solve the Navier–Stokes equations (using the standard constitutive models) as an approximation to the time evolution of the real flow.

The solutions calculated using the multiscale method should converge to the exact solution if we choose $\delta t_{FV}$ to be sufficiently small such that $(\phi^{t+\delta t_{FV}} - \phi^t)/\phi^t \to 0$. In the calculations, we specify a finite $\delta t_{FV}$ so that this expression is $O(1)$ when $|\partial\phi/\partial t|$ is maximum. Using this criterion, we set $\delta t_{FV}/\Delta t_{DSMC} = 20$ for the Rayleigh-flow simulations and $\delta t_{FV}/\Delta t_{DSMC} = 10$ for the Fourier-flow simulations.

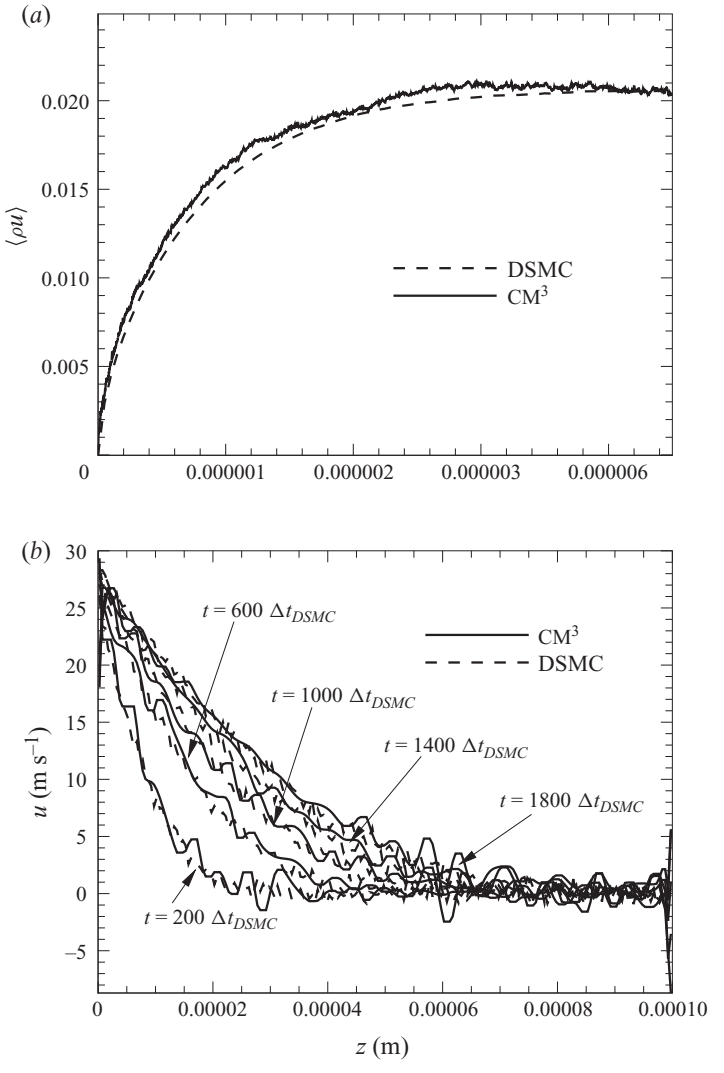


FIGURE 12. (*a*) Unsteady evolution of $\langle \rho u \rangle$ and (*b*) velocity profiles taken at several time instants for the Rayleigh flow with $Kn = 0.02$ (figure 3) calculated using $CM^3$ and DSMC.

As a measure of the temporal evolution of the Rayleigh flow, we define the mean value of the streamwise momentum flux $\langle \rho u \rangle$ as

$$\langle \rho u \rangle = \frac{1}{h} \int_0^h \rho u. \tag{4.3}$$

This quantity, calculated using the $CM^3$ with $\delta t_{FV} = 20 \Delta t_{DSMC}$, is compared to that calculated from an independent DSMC simulation in figure 12(*a*) from time $t = 0$ until the solutions reach a steady state. The actual $u$ and $\tau_{13}$ profiles at several instants in time are shown in figure 12(*b*). We see that the unsteady flow development calculated using the multiscale method is quite similar to the exact (DSMC) evolution.

### 4.3. *Efficiency*

We conclude this section by estimating the computational efficiency of $CM^3$ for the test problems considered above and comparing computational times with those of standard DSMC calculations. In principle, large gains in efficiency compared to DSMC can be attained by taking relatively large advances in time ($\delta t_{FV}$) during the continuum stage of the cycle. This is because the wall clock time spent integrating the continuum equations for a period of time $\Delta t_{DSMC}$, $T_{FV}$, is small compared to the wall clock time required to advance a DSMC simulation forward by the same physical time increment, i.e. $T_{FV} \ll T_{DSMC}$. In practice, the computations are slowed by extra DSMC calculations that are performed during each $CM^3$ cycle to allow $f$ to relax from the initial guess to the correct distribution.

Let $N_1$ be the total number of DSMC time steps used during this maturation period ($N_1 = M \times N_{MC}$), and let $N_2$ be the number of equivalent DSMC time steps taken during the continuum stage of each cycle ($N_2 = \delta t_{FV} / \Delta t_{DSMC}$). Recall that the intent of the DSMC stage of the $CM^3$ cycle is to calculate correct values for $\boldsymbol{\tau}$ and $\boldsymbol{q}$ and not to advance the solution forward in time. Hence, the time advancement is done in the continuum stage, and the number of $CM^3$ cycles that are performed is $Y = N/N_2$, where $N$ is the total number of equivalent DSMC time steps over which the simulation is run. Finally, define $E_{CM^3}$ as the number of ensembles performed for averaging purposes during the Monte Carlo stage of the $CM^3$ and $E_{DSMC}$ as the number of ensembles over which averages are collected in the independent DSMC simulations.

We can then write the estimated ratio of $CM^3$ wall clock time to independent DSMC wall clock time for the same number of time steps, $N$, as

$$E^* = \frac{Y(E_{CM^3} N_1 T_{DSMC})}{E_{DSMC}(N T_{DSMC})} = \frac{(N/N_2)(E_{CM^3} N_1)}{E_{DSMC} N} = \frac{E_{CM^3} N_1}{E_{DSMC} N_2}. \tag{4.4}$$

For the Rayleigh flow (figures 3–5), $E^*$ varied from $O(0.1)$ to $O(1)$, and for the Fourier flow, $E^*$ varied from $O(1)$ to $O(10)$ as $Kn$ was increased from 0.02 to 1. This trend is not surprising, in that we would expect that fewer iterations would be necessary to mature the velocity-distribution function when the true distribution is close to the initial equilibrium distribution used in the calculation. Gains in efficiency can be realized by either integrating for larger increments of time in the continuum stage (larger $\delta t_{FV}$) or by decreasing the number of steps required to reach the proper $f$ in the Monte Carlo stage.

Choosing a value for $\delta t_{FV}$ depends on how quickly the large-scale flow is evolving, and may not be easy to change. There is more room for improvement in setting $N_{MC}$. There would be immediate improvement in efficiency if an adaptive method were used to control $N_1$, so that the maturation process automatically stops when the moments of interest have converged to steady values. Even larger gains can be realized by using an initial distribution that is only a small perturbation from the true distribution at the start of each cycle. One possible method of doing so would be to use the properties of the mature distribution function reached during a previous cycle as an initial distribution in the next cycle. Methods for doing this are currently being developed.

We, however, emphasize that the purpose of this study was to show proof of the multiscale concept and not to produce an optimized algorithm. Hence, the exact values of $E^*$ for these test problems are not entirely representative of the algorithm's efficiency. For instance, the choices of $E_{CM^3}$ and $E_{DSMC}$ do not necessarily produce

equal levels of statistical fluctuations, but the values used here allowed the fluctuations in the computed solutions to be comparable. Adjusting these values would lead to small changes in the computed $E^*$. The $CM^3$ also offers a potential advantage if it is used as part of a larger spatial hybrid method, since the continuum variables at interfaces between rarefied and continuum regions are available and can be used for coupling the two regions. A proper analysis of the efficiency needs to take this application into consideration.

## 5. Conclusions

We have introduced a multiscale method for transition-regime gas flows and discussed the operational details of implementation. The $CM^3$ uses a finite-volume method to solve the generalized conservation equations with components of the stress tensor and heat-flux vector calculated from molecular velocity fluctuations obtained from a Monte Carlo simulation of the Boltzmann equation. These 'instantaneous' closure relations take the place of constitutive models that are generally used to develop continuum-level equations.

The $CM^3$ was used to calculate a low-speed Rayleigh flow at three different values of $Kn$. Steady-state velocity and shear-stress profiles compared well with DSMC solutions for all three $Kn$. Even for the most rarefied flow, $Kn = 1$, for which the Navier–Stokes equations are no longer valid, the $CM^3$ produced solutions that quantitatively match DSMC solutions. The ability of the $CM^3$ to calculate unsteady flows was also tested. The time evolution of a low-$Kn$ flow calculated using $CM^3$ was found to be comparable to that calculated with DSMC. The small deviations that were observed could be decreased by using smaller $\delta t_{FV}$ but at a greater computational cost. Likewise, the statistical fluctuations in the $CM^3$ profiles could be reduced by fine-tuning the smoothness factor, $f_s$, in the B-spline interpolations or by using a more sophisticated noise-reduction method. Both improvements come at increased computational cost.

Similar comparisons of the steady-state temperature and wall-normal heat-flux profiles for a stationary Fourier flow calculated using $CM^3$, DSMC and the Navier–Stokes equations were made. Good agreement among all methods was found for small $Kn$. For larger $Kn$, the $CM^3$ temperature profiles agreed well with the DSMC solutions.

Details of implementing this multiscale method were discussed. Some knowledge about the physics of the flow is necessary to properly specify the various length and time scales of the solution algorithm. In particular, *a priori* estimates of the statistical variation in the molecular velocities, the maximum rate of change of the continuum flow field and the level of rarefaction of the gas can be used to determine proper values for the smoothing factor of the B-spline interpolants $f_s$, the maximum size of the continuum step that can be taken each cycle $\delta t_{FV}$ and the number of Monte Carlo iterations required to mature the initial velocity distribution to the correct $f$ during each cycle, $N_{MC}$, respectively. The latter two time scales directly control the efficiency of the algorithm. For the Rayleigh flow, the calculation times using the multiscale method varied from less than one (more efficient) to of the same order as standard DSMC calculations. For the Fourier flow, the multiscale solutions were more expensive because of slow convergence of the heat-flux vector.

The calculations presented here represent the first steps towards building an efficient and flexible multiscale simulation procedure for rarefied gas flows. Improvements in algorithmic efficiency can be made in a variety of ways. For instance, $N_{MC}$ could

be dynamically controlled throughout the course of a simulation by monitoring the convergence time for $\boldsymbol{\tau}$ and $\boldsymbol{q}$ during each Monte Carlo continuum cycle, and, similarly, $\delta t_{FV}$ could also be changed dynamically based on the rate of change of the continuum flow field. Significantly improving the computational efficiency, particularly for large-$Kn$ flows, will require developing better methods for specifying the initial velocity distributions at the beginning of each cycle and thus reducing the number of iterations needed for the moments to converge. A more thorough analysis considering the $CM^3$ as part of a larger spatial hybrid method is needed to properly evaluate the efficiency of this methodology. Even if the individual $CM^3$ regions in such a method are slightly more expensive than DSMC, the availability of continuum quantities at the interfaces between the rarefied and continuum regions will facilitate coupling between these regions and may lead to improvements in overall efficiency. In order to do so, the method must still be extended to multiple dimensions, and proper boundary conditions must be derived. Such issues will be addressed in a future publication.

We would like to thank the National Academies of Science Postdoctoral Research Associateship Program and the Naval Research Laboratory through the Office of Naval Research for funding this work. Computing resources were provided by the DoD High Performance Computing Modernization Program. We would also like to thank Dr J. Lui for assistance with implementing LCPFCT, Dr D. Mott for valuable insight regarding DSMC boundary conditions and Dr A. Staples for general information regarding multiscale methods.

## REFERENCES

Al-Mohssen, H. A., Hadjiconstantinou, N. G. & Kevrekidis, I. G. 2007 Acceleration methods for coarse-grained numerical solution of the Boltzmann equation. *ASME J. Fluid Engng* **129**, 908–912.

van Albada, G. D., van Leer, B. & Roberts, W. W. 1982 A comparative study of computational methods in cosmic gas dynamics. *Astron. Astrophys.* **108**, 76–84.

Andullah, L. S. & Babovsky, H. 2003 A discrete Boltzmann equation based on hexagons. *Math. Models Methods Appl. Sci.* **13**, 1537–1563.

Ansumali, S. & Karlin, I. V. 2002 Kinetic boundary conditions in the lattice Boltzmann method. *Phys. Rev.* E **66**, 026311.

Ansumali, S. & Karlin, I. V. 2005 Consistent lattice Boltzmann method. *Phys. Rev. Lett.* **95**, 260605.

Ansumali, S., Karlin, I. V., Arcidiacono, S., Abbas, A. & Pasianakis, N. I. 2007 Hydrodynamics beyond Navier–Stokes: exact solution to the lattice Boltzmann hierarchy. *Phys. Rev. Lett.* **98**, 124502.

Babovsky, H. 1998 Discretization and numerical schemes for steady kinetic model equations. *Comput. Math. Appl.* **35**, 29–40.

Baker, L. L. & Hadjiconstantinou, N. G. 2005 Variance reduction for Monte Carlo solutions of the Boltzmann equation. *Phys. Fluids* **17**, 051703.

Benzi, R., Succi, S. & Vergassola, M. 1992 The lattice Boltzmann equation: theory and applications. *Phys. Rep.* **222**, 145–197.

Bird, G. A. 1994 *Molecular Gas Dynamics and the Direct Simulation of Gas Flows*. Oxford Science Publications.

Boris, J., Landsberg, A., Oran, E. S. & Gardner, J. 1993 LCPFCT: a flux-corrected transport algorithm for solving generalized continuity equations. *Memorandum Rep.* 6410-93-7192, US Naval Research Laboratory, Washington, DC.

Bourgat, J. F., Le Tallec, P. & Tidriri, M. D. 1996 Coupling Boltzmann and Navier–Stokes equations by friction. *J. Comput. Phys.* **127**, 227–245.

Broadwell, J. E. 1964 Study of rarefied flow by the discrete velocity method. *J. Fluid Mech.* **19**, 401–414.

Cercignani, C. 1975 *Theory and Applications of the Boltzmann Equation*. Elsevier.

Chikatamarla, S. S. & Karlin, I. V. 2006 Entropy and Galilean invariance of lattice Boltzmann theories. *Phys. Rev. Lett.* **97**, 190601.

Chun, J. & Koch, D. 2005 A direct simulation Monte Carlo method for rarefied gas flows in the limit of small Mach number. *Phys. Fluids* **17**, 87–132.

Degond, P. & Jin, S. 2005 A smooth transition model between kinetic and diffusion equations. *SIAM J. Numer. Anal.* **42**, 2671–2687.

Degond, P., Jin, S. & Mieussens, L. 2005 A smooth transition model between kinetic and hydrodynamic equations. *J. Comput. Phys.* **209**, 665–694.

Degond, P., Liu, J.-G. & Mieussens, L. 2006 Macroscopic fluid models with localized kinetic upscaling effects. *Multiscale Model. Simul.* **5**, 940–979.

Deshpande, S. M. 1986 Kinetic-theory based method for inviscid compressible flows. *Tech. Paper* 2613. NASA Langley.

Dierckx, P. 1975 An algorithm for smoothing, differentiation and integration of experimental data using spline functions. *J. Comput. Appl. Math.* **1**, 165–184.

Dierckx, P. 1982 A fast algorithm for smoothing data on a rectangular grid while using spline functions. *SIAM J. Numer. Anal.* **19**, 1286–1304.

Dierckx, P. 1993 *Curve and Surface Fitting with Splines*. Monographs on Numerical Analysis, Oxford University Press.

Doolen, G. D. (Ed.) 1990 *Lattice Gas Methods for Partial Differential Equations*. Addison-Wesley.

E, W. & Engquist, B. 2003 The heterogeneous multiscale methods. *Commun. Math. Sci.* **1**, 87–132.

Fan, J. & Shen, C. 2001 A direct simulation method for subsonic, microscale gas flows. *J. Comput. Phys.* **167**, 393–412.

Fiscko, K. A. & Chapman, D. R. 1989 Comparison of Burnett, super-Burnett and Monte Carlo solutions for hypersonic shock structure. *Prog. Aeronaut. Astronaut.* **118**, 374–395.

Garcia, A. L., Bell, J. B., Crutchfield, W. Y. & Alder, B. J. 1999 Adaptive mesh and algorithm refinement using direct simulation Monte Carlo. *J. Comput. Phys.* **154**, 134–155.

Gatignol, R. 1970 Théorie cinétique d'un gaz à répartition discrète de vitesses. *Z. Flugwiss.* **18**, 93–97.

Goldstein, D., Sturtevant, B. & Broadwell, J. E. 1989 Investigation of the motion of discrete-velocity gases. *Prog. Astronaut. Aeronaut.* **118**, 100–117.

Gorban, A. N., Karlin, I. V. & Zinovyev, A. Y. 2004 Constructive methods of invariant manifolds for kinetic problems. *Phys. Rep.* **396**, 197–403.

Grad, H. 1949 On the kinetic theory of rarefied gases. *Commun. Pure Appl. Math.* **2**, 331–407.

Harten, A., Lax, P. D. & van Leer, B. 1983 On upstream differencing and Godunov-type schemes for hyperbolic conservation laws. *SIAM Rev.* **25**, 35–61.

Higuera, F. J. & Jimenez, J. 1989 Boltzmann approach to lattice gas simulations. *Europhys. Lett.* **9**, 663–668.

Homolle, T. M. M. & Hadjiconstantinou, N. G. 2007 A low-variance deviational simulation Monte Carlo for the Boltzmann equation. *J. Comput. Phys.* **226**, 2341–2358.

Kaplan, C. R. & Oran, E. S. 2002 Nonlinear filtering for low-velocity gaseous microflows. *AIAA J.* **40**, 82–90.

Karlin, I. V., Gorban, A. N., Dukek, G. & Nonnenmacher, T. F. 1998 Dynamic correction to moment approximations. *Phys. Rev.* E **57**, 1668–1672.

Kevrekidis, I. G., Gear, C. W. & Hummer, G. 2004 Equation-free: the computer-assisted analysis of complex, multiscale systems. *AICHE J.* **50**, 1346–1355.

Kevrekidis, I. G., Gear, C. W., Hyman, J. M., Kevrekidis, P. G., Runborg, O. & Theodoropoulos, K. 2003 Equation-free coarse-grained multiscale computation: enabling macroscopic simulators to perform system-level tasks. *Commun. Math. Sci.* **1**, 715–762.

Kim, S. H., Pitsch, H. & Boyd, I. D. 2008 Accuracy of higher order lattice Boltzmann methods for microscale flows with finite Knudsen numbers. *J. Comput. Phys.* **227**, 8655–8671.

Laso, M. & Ottinger, H. C. 1993 Calculation of viscoelastic flow using molecular models: the CONNFESSIT approach. *J. Fluid Mech.* **47**, 1–20.

Le Tallec, P. & Mallinger, F. 1997 Coupling Boltzmann and Navier–Stokes equations by half fluxes. *J. Comput. Phys.* **136**, 51–67.

Lian, Y.-Y., Wu, J.-S., Cheng, G. & Koomullil, R. 2005 Development of a parallel hybrid method for the DSMC and Navier–Stokes solver. *AIAA Paper* 2005-0435.

Macrossan, M. N. 1989 The equilibrium flux method for the calculation of flows with non-equilibrium chemical reactions. *J. Comput. Phys.* **80**, 204–231.

McNamara, G. R. & Zanetti, G. 1988 Use of the Boltzmann equation to simulate lattice-gas automata. *Phys. Rev. Lett.* **61**, 2332–2335.

Mieussens, L. 2000 Discrete-velocity models and numerical schemes for the Boltzmann–BGK equation in plane and axisymmetric geometries. *J. Comput. Phys.* **162**, 429–466.

Nordsieck, A. & Hicks, B. L. 1967 Monte Carlo evaluation of the Boltzmann collision integral. In *Rarefied Gas Dynamics* (ed. L. Brundin), pp. 675–710. Academic.

Oran, E. S. & Boris, J. P. 2001 *Numerical Simulation of Reactive Flows*. Elsevier.

Oran, E. S., Oh, C. K. & Cybyk, B. 1998 Direct simulation Monte Carlo: recent advances and applications. *Annu. Rev. Fluid Mech.* **30**, 403–441.

Pan, L., Ng, T. & Lam, K. 2001 Molecular block model direct simulation Monte Carlo method for low velocity microgas flows. *J. Micromech. Mircroengng* **11**, 181–188.

Panton, R. L. 1996 *Incompressible Flow*. Wiley–Interscience.

Perthame, B. 1992 Second-order Boltzmann schemes for compressible Euler equations in one and two space dimensions. *SIAM J. Numer. Anal.* **29**, 1–19.

Pham-Van-Diep, G. C., Erwin, D. A. & Muntz, E. P. 1991 Testing continuum descriptions of low-Mach-number shock structures. *J. Fluid Mech.* **232**, 403–413.

Plapp, M. & Karma, A. 2000 Multiscale finite-difference-diffusion-Monte-Carlo method for simulating dendritic solidification. *J. Comput. Phys.* **165**, 592–619.

Prendergast, K. H. & Xu, K. 1993 Numerical hydrodynamics from gas-kinetic theory. *J. Comput. Phys.* **109**, 53–66.

Pullin, D. I. 1980 Direct simulation methods for compressible inviscid ideal-gas flow. *J. Comput. Phys.* **34**, 231–244.

Qian, Y. H., d'Humières, D. & Lallemand., P. 1992 Lattice BGK models for Navier–Stokes equation. *Europhys. Lett.* **17**, 479–484.

Reitz, R. D. 1981 One-dimensional compressible gas dynamics calculations using the Boltzmann equation. *J. Comput. Phys.* **42**, 108–123.

Roveda, R., Goldstein, D. B. & Varghese, P. L. 2000 Hybrid Euler/particle approach for continuum/rarefied flows. *J. Spacecr. Rockets* **35**, 258–265.

Sanders, R. H. & Prendergast, K. H. 1974 The possible relation of the 3-kiloparsec arm to explosions in the galactic nucleus. *Astrophys. J.* **188**, 489–500.

Schwartzentruber, T. E. & Boyd, I. D. 2006 A hybrid particle-continuum method applied to shock waves. *J. Comput. Phys.* **215**, 402–416.

Shen, C., Tian, D. B., Xie, C. & Fan, J. 2004 Examination of the LBM in simulations of microchannel flow in transitional regime. *Microscale Thermophys. Engng* **8**, 423–432.

Steger, J. L. & Warming, R. F. 1981 Flux vector splitting of the inviscid gas dynamic equations with application to finite-difference methods. *J. Comput. Phys.* **40**, 263–293.

Struchtrup, H. & Torrilhon, M. 2003 Regularization of Grad's 13 moment equations: derivation and linear analysis. *Phys. Fluids* **15**, 2668.

Sun, Q. & Boyd, I. 2002 Statistical simulation of low-speed rarefied gas flows. *J. Comput. Phys.* **179**, 400–425.

Theodoropoulos, K., Qian, Y. H. & Kevrekidis, I. G. 2000 'Coarse' stability and bifurcation analysis using time-steppers: a reaction–diffusion example. *Proc. Natl. Acad. Sci.* **97**, 9840–9843.

Torrilhon, M. & Struchtrup, H. 2004 Regularized 13-moment equations: shock structure calculations and comparison to Burnett models. *J. Fluid Mech.* **513**, 171.

Verhaeghe, F., Luo, L.-S. & Blanpain, B. 2009 Lattice Boltzmann modeling of microchannel flow in slip flow regime. *J. Comput. Phys.* **228**, 147–157.

Wadsworth, D. C. & Erwin, D. A. 1992 Two-dimensional hybrid continuum/particle approach for rarefied flows. *AIAA Paper* 92-2975.

Wagner, W. 1992 A convergence proof for Bird's direct simulation Monte Carlo method for the Boltzmann equation. *J. Statist. Phys.* **66**, 1011–1044.

Watari, M. 2009 Velocity slip and temperature jump simulations by the three-dimensional thermal finite-difference lattice Boltzmann method. *Phys. Rev.* E **79**, 066706.

Wijesinghe, H. S., Hornung, R. D., Garcia, A. L. & Hadjiconstantinou, N. G. 2004 Three-dimensional hybrid continuum-atomistic simulations for multiscale hydrodynamics. *ASME J. Fluids Engng* **126**, 768–777.

Xu, K. & Prendergast, K. 1994 Numerical Navier–Stokes solutions from gas kinetic theory. *J. Comput. Phys.* **114**, 9–17.

Yasuda, S. & Yamamoto, R. 2010 Multiscale modeling and simulation for polymer melt flows between parallel plates. *Phys. Rev.* E **81**, 036308.

Yen, S.-M. 1971 Monte Carlo solutions of nonlinear Boltzmann equation for problems of heat transfer in rarefied gases. *Intl J. Heat Mass Transfer* **14**, 1865–1869.

Yen, S. M. 1984 Numerical solution of the nonlinear Boltzmann equation for nonequilibrium gas flow problems. *Annu. Rev. Fluid Mech.* **16**, 67–97.